



## 저작자표시-비영리-변경금지 2.0 대한민국

이용자는 아래의 조건을 따르는 경우에 한하여 자유롭게

- 이 저작물을 복제, 배포, 전송, 전시, 공연 및 방송할 수 있습니다.

다음과 같은 조건을 따라야 합니다:



저작자표시. 귀하는 원저작자를 표시하여야 합니다.



비영리. 귀하는 이 저작물을 영리 목적으로 이용할 수 없습니다.



변경금지. 귀하는 이 저작물을 개작, 변형 또는 가공할 수 없습니다.

- 귀하는, 이 저작물의 재이용이나 배포의 경우, 이 저작물에 적용된 이용허락조건을 명확하게 나타내어야 합니다.
- 저작권자로부터 별도의 허가를 받으면 이러한 조건들은 적용되지 않습니다.

저작권법에 따른 이용자의 권리는 위의 내용에 의하여 영향을 받지 않습니다.

이것은 [이용허락규약\(Legal Code\)](#)을 이해하기 쉽게 요약한 것입니다.

[Disclaimer](#)

PH.D. DISSERTATION

MODELING METHODOLOGY OF  
PULSE-ECHO ULTRASOUND SYSTEM FOR  
MEDICAL IMAGING DIAGNOSTICS

의료 영상 진단을 위한 펄스-에코 초음파 시스템의  
모델링 방법론

BY

TAEHOON KIM

FEBRUARY 2017

DEPARTMENT OF ELECTRICAL ENGINEERING AND  
COMPUTER SCIENCE  
COLLEGE OF ENGINEERING  
SEOUL NATIONAL UNIVERSITY

MODELING METHODOLOGY OF  
PULSE-ECHO ULTRASOUND SYSTEM FOR  
MEDICAL IMAGING DIAGNOSTICS

의료 영상 진단을 위한 펄스-에코 초음파 시스템의  
모델링 방법론

지도교수 김 수 환

이 논문을 공학박사 학위논문으로 제출함

2017년 2 월

서울대학교 대학원

전기컴퓨터 공학부

김 태 훈

김태훈의 공학박사 학위논문을 인준함

2017년 2 월

위 원 장 : 정덕균 (印)

부위원장 : 김수환 (印)

위 원 : 심병호 (印)

위 원 : 이종호 (印)

위 원 : 이현중 (印)

# ABSTRACT

## MODELING METHODOLOGY OF PULSE-ECHO ULTRASOUND SYSTEM FOR MEDICAL IMAGING DIAGNOSTICS

TAEHOON KIM  
DEPARTMENT OF ELECTRICAL ENGINEERING AND  
COMPUTER SCIENCE  
COLLEGE OF ENGINEERING  
SEOUL NATIONAL UNIVERSITY

A flexible clinical ultrasound system must operate with different transducers, which have characteristic impulse responses and widely varying impedances. The impulse response determines the shape of the high-voltage pulse that is transmitted and the specifications of the front-end electronics that receive the echo; and the impedance determines the specification of the matching network through which the transducer is connected. System-level optimization of these subsystems requires accurate modeling of pulse-echo (two-way) response, which in turn demands a unified simulation of the ultrasonics and electronics.

This thesis proposed modeling methodology of pulse-echo ultrasound system for medical imaging diagnostics and the development of pulse-echo ultrasound system simulator in the Matlab/Simulink environment by using the modeling methodology. This simulator is realized by combining Matlab/Simulink models of the high-voltage

transmitter, the transmission interface, the acoustic subsystem which includes wave propagation and reflection, the receiving interface, and the front-end receiver.

To demonstrate the effectiveness of our simulator, the models are experimentally validated by comparing the simulation results with the measured data from commercial ultrasound system. Proposed pulse-echo ultrasound simulator, which is developed by our modeling methodology, could be used to quickly provide system-level feedback for an optimized tuning of electronic design parameters.

**Keywords:** ultrasound imaging, ultrasound transducer, behavior modeling, design optimization, impedance matching, MATLAB.

**Student Number:** 2012-30202

# CONTENTS

<b>ABSTRACT .....</b>	<b>I</b>
<b>CONTENTS .....</b>	<b>IV</b>
<b>LIST OF FIGURES .....</b>	<b>VIII</b>
<b>LIST OF TABLES.....</b>	<b>XI</b>
<b>CHAPTER 1 INTRODUCTION .....</b>	<b>1</b>
1.1 ULTRASOUND IMAGING.....	1
1.2 HISTORY OF ULTRASOUND IMAGING .....	5
1.3 CHALLENGE AND APPROACH.....	8
1.4 THESIS ORGANIZATION .....	11
<b>CHAPTER 2 FUNDAMENTALS OF ULTRASOUND SYSTEMS.....</b>	<b>12</b>
2.1 BASIC ULTRASOUND PHYSICS .....	12
2.1.1 SOUND WAVES.....	12
2.1.2 REFLECTION.....	15
2.1.3 SCATTERING.....	18
2.1.4 REFRACTION .....	19
2.1.5 DIFFRACTION .....	21
2.1.6 ABSORPTION .....	22
2.1.7 ATTENUATION.....	24

2.2	ULTRASOUND SYSTEM OVERVIEW .....	26
2.3	PIEZOELECTRIC TRANSDUCER .....	29
2.4	HIGH-VOLTAGE TRANSMITTER .....	32
2.5	FRONT-END RECEIVER .....	33
<b>CHAPTER3</b>	<b>MODELING OF ULTRASOUND TRANSDUCER.....</b>	<b>35</b>
3.1	THEORETICAL MODELS .....	35
3.1.1	LEACH MODEL .....	35
3.1.2	ACOUSTICAL ATTENUATION.....	38
3.1.3	PROPAGATING MEDIUM.....	42
3.1.4	DIFFRACTION EFFECTS .....	44
3.1.5	PARASITIC COMPONENTS.....	45
3.2	BUTTERWORTH VAN-DYKE MODEL .....	47
3.3	ANALYTICAL MODEL .....	52
<b>CHAPTER4</b>	<b>DEVELOPMENT OF MATLAB/SIMULINK PULSE-ECHO ULTRASOUND SYSTEM SIMULATOR.....</b>	<b>56</b>
4.1	MODELING STRATEGY FOR PULSE-ECHO ULTRASOUND SYSTEM.....	56
4.2	HIGH-VOLTAGE TRANSMITTER MODEL.....	60
4.3	ACOUSTIC SUBSYSTEM AND INTERFACING ELECTRONICS MODELS.....	62
4.4	FRONT-END RECEIVER MODEL.....	67
4.4.1	T/R SWITCH AND ACTIVE TERMINATION .....	67
4.4.2	HARMONIC DISTORTION .....	70
4.4.3	AMPLIFIER AND FILTER .....	72
4.4.4	SAMPLING CLOCK JITTER .....	74
4.4.5	ANALOG-TO-DIGITAL CONVERTER.....	76
<b>CHAPTER5</b>	<b>EXPERIMENTS VERSUS SIMULATION.....</b>	<b>78</b>
5.1	VALIDATION OF SUBSYSTEMS .....	78

5.1.1 ACOUSTIC SUBSYSTEM AND INTERFACING ELECTRONICS .....	78
5.1.2 FRONT-END RECEIVER .....	83
5.2 VALIDATION OF COMPLETE SYSTEM .....	87
5.2.1 EXPERIMENTAL SETUP .....	87
5.2.2 COMPARISON SIMULATION AND MEASUREMENTS .....	91
5.3 DISCUSSION .....	95
<b>CHAPTER6 CONCLUSIONS .....</b>	<b>97</b>
<b>BIBLIOGRAPHY.....</b>	<b>99</b>
<b>ABSTRACT IN KOREAN.....</b>	<b>105</b>



# LIST OF FIGURES

Fig. 1.1.1	Acoustic spectrum .....	3
Fig. 2.1.1	Reflection caused by a sound wave striking a large smooth interface at normal incidence.....	15
Fig. 2.1.2	Nonspecular reflection (scattering) .....	18
Fig. 2.1.3	Case of refraction. ....	19
Fig. 2.1.4	Divergence of a sound beam from a small source.....	20
Fig. 2.1.5	Attenuation of acoustic pressure as a sound beam penetrates the medium.....	22
Fig. 2.2.1	Ultrasound system block diagram. ....	26
Fig. 2.3.1	Structure of a typical piezoelectric transducer. ....	29
Fig. 3.1.1	Leach model, analog circuit for the thickness-mode transducer .....	35
Fig. 3.1.2	Lumped segment of the lossy transmission line.....	37
Fig. 3.1.3	Spice model of the lossy thickness-mode transducer .....	39
Fig. 3.1.4	Schematic used for simulation of parasitic components .....	44
Fig. 3.2.1	Impedance measurement setup for ultrasound transducer .....	46
Fig. 3.2.2	Schematic diagrams of (a) conventional and (b) modified BVD models ..	47
Fig. 3.3.1	Analytical model of the ultrasound transducer.....	51
Fig. 3.3.2	Block diagram of the experimental setup.....	52
Fig. 4.1.1	Block diagram of a pulse-echo ultrasound system .....	55
Fig. 4.1.2	Model of the pulse-echo ultrasound system. ....	56
Fig. 4.2.1	Simulink model of the high-voltage transmitter.....	58
Fig. 4.3.1	Setup for the pulse-echo measurements required to build the electroacoustic transfer function $H(s)$ . ....	61
Fig. 4.3.2	Simulink models of the TX interfacing electronics, acoustic subsystem, and	

	RX interfacing electronics, based respectively on the transfer functions $Z_{TX}(s)$ , $H(s)$ , and $Z_{RX}(s)$ .....	62
Fig. 4.4.1	Simulink model of the front-end receiver .....	65
Fig. 4.4.2	Equivalent circuit model of the T/R switch under considering the active input termination.....	66
Fig. 4.4.3	Simulink model of harmonic distortion .....	68
Fig. 4.4.4	Simulink model of LNA, VCAT and VGA with variable gain.....	69
Fig. 4.4.5	Simulink model of HPF and LPF with selective bandwidth .....	69
Fig. 4.4.6	Simulink model of sampling clock jitter .....	70
Fig. 4.4.7	Sampling clock jitter .....	71
Fig. 4.4.8	Simulink model of ADC .....	72
Fig. 4.4.9	Simulink model of input SHA in ADC .....	73
Fig. 4.4.10	Simulink model of MDAC in $i$ th stage .....	73
Fig. 4.4.11	Simulink model of sub-ADC in $i$ th stage.....	73
Fig. 5.1.1	Comparison between the transfer function $Z_{TX}(s)$ and the experimental data $Z_{TX}(j2\pi f_k)$ (a) magnitude and (b) phase, both against the frequency $f_k$ .....	76
Fig. 5.1.2	Comparison between the transfer function $H(s)$ and the experimental data $H(j2\pi f_k)$ (a) magnitude and (b) phase, both against the frequency $f_k$ .....	77
Fig. 5.1.3	Comparison between the transfer function $Z_{RX}(s)$ and the experimental data $Z_{RX}(j2\pi f_k)$ (a) magnitude and (b) phase, both against the frequency $f_k$ .....	78
Fig. 5.2.1	Photographs of (a) our experimental setup with (b) the water tank.....	84
Fig. 5.2.2	Block diagram of a pulse-echo ultrasound system in (a) transmit and (b) receive mode .....	85
Fig. 5.2.3	Measured and simulated amplitudes of the high-voltage pulse $V(1)$ .....	87
Fig. 5.2.4	Measured and simulated amplitudes of the echo signal $V(2)$ (a) in the time domain and (b) in the frequency domain .....	88
Fig. 5.2.5	Measured and simulated amplitude of the digitized output $V(3)$ (a) in the time domain and (b) in the frequency domain.....	89

# LIST OF TABLES

Table 1.1.1	Comparison of imaging modalities.....	2
Table 2.1.1	Acoustic impedance of some main biological tissues.....	17
Table 2.1.2	Attenuation of human tissues and other media at 1MHz.....	24
Table 5.1.1	Front-end receiver parameters in the Matlab/Simulink model.....	80
Table 5.1.2	Measured and simulated values of NBSNR of the front-end receiver for different combinations of LNA and PGA gain, and with different termination resistors.....	81
Table 5.1.3	Measured and simulated values of SFDR of the front-end receiver for different combinations of LNA and PGA gain, and with different termination resistors.....	82

# CHAPTER 1

## INTRODUCTION

### 1.1 ULTRASOUND IMAGING

Ultrasound techniques are widely used for numerous applications, such as SONAR (Sound Navigation and Ranging), diagnostic imaging, nondestructive testing, and surface acoustic wave (SAW) devices, etc.

Ultrasound medical imaging devices are widely used as medical diagnosis tools. Millions of people have been spared painful exploratory surgery by noninvasive imaging. Their lives have been saved by ultrasound diagnosis and timely intervention, their hearts have been evaluated and repaired, and their children have been guided and checked by ultrasound. Many more people have breathed a sigh of relief after a brief ultrasound exam found no disease or confirmed the health of their future child.

Compared to X-ray and computer tomography (CT) devices, which expose the human body to radiation, the ultrasound medical imaging is harmless to the human body. Also, it is noninvasive and less costly than other cross-sectional imaging modalities such as CT and magnetic resonance imaging (MRI). Table 1.1.1 shows comparison of imaging modalities [1.1.1].

Table 1.1 Comparison of imaging modalities

<b>Modality</b>	<b>Ultrasound</b>	<b>X-ray</b>	<b>CT</b>	<b>MRI</b>
What is imaged	Mechanical properties	Mean tissue absorption	Tissue absorption	Biochemistry
Spatial resolution	0.3-3 mm	~1 mm	~1 mm	~1 mm
Penetration	3-25 cm	Excellent	Excellent	Excellent
Safety	Very good	Ionizing radiation	Ionizing radiation	Very good
Speed	100 frames/sec	Minutes	1/2 minute to minutes	10 frames/sec
Cost	cheap	cheap	expensive	Very expensive
Portability	Excellent	Good	Poor	Poor

Mechanical waves and vibrations occur over a wide range of frequencies called the acoustic spectrum. This spectrum extends from the audible range (10 to 20,000 Hz), with which we are all familiar, to the range of phonons ( $>10^{12}$  Hz), which comprise the vibrational states of matter. A graphical interpretation of the acoustic spectrum is given in Fig. 1.1.1 [1.1.2], in which frequency is shown in powers of 10 on the horizontal axis from  $10^0$  to  $10^{13}$  Hz. Sound occupies the range from 10 Hz to 20 KHz. We are all familiar

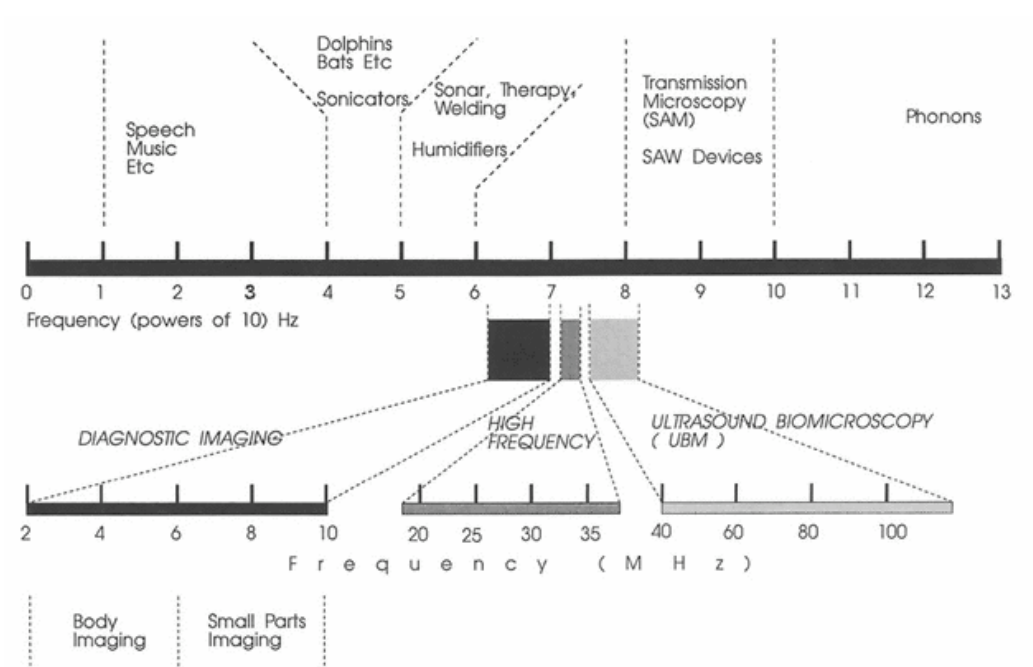


Fig. 1.1.1. The acoustic spectrum. Diagnostic applications are clustered in the 1-10MHz range, whereas ultrasound bio-microscopy applications occur in the range from approximately 40 to 100MHz.

with the fabulous wealth of information that we extract from verbal communication, music, and other sources of sound. It is not surprising, therefore, that frequencies greater than 20 KHz, the ultrasound frequencies, have similar potential. In the frequency range from 20 to 100 KHz many animals use ultrasound to communicate and navigate and to track their prey.

From 100 KHz ( $10^5$  Hz) to 1MHz ( $10^6$  Hz), ultrasound has numerous applications. Perhaps the most important of these is SONAR, which is the human imitation of the echolocation methods of many animals. The medical applications occupy only a tiny

silver of the spectrum between 1 and 10MHz. Even in this range the choice of frequency is closely tied to the intended application. For example, frequencies between 3.5 and 5MHz are used in body imaging applications where significant penetration of the tissues is needed. These frequencies have the ability to penetrate the tissues to a depth of 15 to 20cm and still return signals of sufficient strength to form an image. As the frequency increases, the ultrasound is more strongly attenuated, reducing penetration. Higher frequencies (7 to 10MHz) can be used in small parts imaging such as visualization of the eye, where penetration of 4 to 5cm is sufficient.

Although the vast majority of clinical ultrasound imaging is performed between 1 and 10MHz, new applications are beginning to emerge in the high-frequency range between 10 and 40MHz. These include systems designed to image the skin, imaging of blood vessels. The commercial systems for skin and intravascular applications in the 20 to 30MHz range have transverse resolution ranging from approximately 200 to 500 $\mu$ m and are still considered experimental.

## **1.2 HISTORY OF ULTRASOUND IMAGING**

The concept of deriving real-time parameters other than direct pulse-echo data by signal processing or by displaying data in different ways was not obvious at the very beginning of medical ultrasound. M-mode, or a time-motion display, presented new time-varying information about heart motion at a fixed location when I. Elder and C. H. Hertz introduced it in 1954. In 1955, S. Satomura, Y. Nimura, and T. Yoshida reported experiments with Doppler-shifted ultrasound signals produced by heart motion. Doppler signals shifted by blood movement fall in the audio range and can be heard as well as seen on a display. By 1966, D. Baker and V. Simmons had shown that pulsed spectral Doppler was possible (Goldberg and Kimmelman, 1988). P. N. T. Wells (1969) invented a range-gated Doppler to isolate different targets.

In the early 1980s, Eyer et al. (1981) and Namekawa et al. (1982) described color flow imaging techniques for visualizing the flow of blood in real time. During the late 1980s, many other signal processing methods for imaging and calculations began to appear on imaging systems. Concurrently, sonar systems evolved to such a point that Dr. Robert Ballard was able to discover the Titanic at the bottom of the sea with sonar and video equipment in 1986 (Murphy, 1986).

Also during the 1980s, transducer technology underwent tremendous growth. Based on the Mason equivalent circuit model and waveguide, as well as the matching-layer design technology and high coupling piezoelectric materials developed during and after World War II, ultrasonic phased array design evolved rapidly. Specialized phased and



linear arrays were developed for specific clinical applications: ardiogy; radiology (noncardiac internal organs); obstetrics/gynecology and transvaginal; endoscopic (transducer manipulated on the tip of an endoscope); transesophageal (transducer down the esophagus) and transrectal; surgical, intraoperative (transducer placed in body during surgery), laparoscopic, and neurosurgical; vascular, intravascular, and small parts. With improved materials and piezoelectric composites, arrays with several hundred elements and higher frequencies became available. Wider transducer bandwidths allowed the imaging and operation of other modes within the same transducer at several frequencies selectable by the user.

By the 1990s, developments in more powerful microprocessors, high-density gate arrays, and surface mount technology, as well as the availability of low-cost analog/digital (A/D) chips, made greater computation and faster processing in smaller volumes available at lower costs. Imaging systems incorporating these advances evolved into digital architectures and beamformers. Broadband communication enabled the live transfer of images for telemedicine. Transducers appeared with even wider bandwidths and in 1.5D (segmented arrays with limited elevation electronic focusing capabilities) and matrix array configurations.

By the late 1990s, near-real-time three-dimensional (3D) imaging became possible. Commercial systems mechanically scanned entire electronically scanned arrays in ways similar to those used for single-element mechanical scanners. Translating, angular fanning, or spinning an array about an axis created a spatially sampled volume. Special image-processing techniques developed for movies such as John Cameron's Titanic

enabled nearly real-time three-dimensional imaging, including surface-rendered images of fetuses.

To extend the capabilities of ultrasound imaging, contrast agents were designed to enhance the visibility of blood flow. In 1968, Gramiak and Shah discovered that microbubbles from indocyanine green dye injected in blood could act as an ultrasound contrast agent. By the late 1980s, several manufacturers were developing contrast agents to enhance the visualization of and ultrasound sensitivity to blood flow. To emphasize the detection of blood flow, investigators imaged contrast agents at harmonic frequencies generated by the microbubbles. As imaging system manufacturers became involved in imaging contrast agents at second harmonic frequencies, they discovered that tissues could also be seen. Signals sent into the body at a fundamental frequency returned from tissue at harmonic frequencies. Tissues talked back. P. N. T. Wells (1969a) mentioned indications that tissues had nonlinear properties. Some work on imaging the nonlinear coefficient of tissues directly (called their “B/A” value) was done in the 1980s but did not result in manufactured devices. By the late 1990s, the clinical value of tissue harmonic imaging was recognized and commercialized. Tissue harmonic images have proved to be very useful in imaging otherwise difficult-to-image people, and in many cases, they provide superior contrast resolution and detail compared with images made at the fundamental frequency.

## 1.3 CHALLENGE AND APPROACH

Ultrasound imaging has been applied to many clinical applications, including obstetrics, gynecology, orthopedics, emergency medicine and the detection of cancer. Ultrasound imaging provides immediate data, facilitating speedy diagnosis and reducing cost. The type of transducer required varies across different applications, and transducers commonly have different impedance values and impulse responses. For example, an annular array transducer is required for steerable continuous-wave Doppler measurements of the heart, whereas an array with a tight convex curvature is required for imaging between the ribs [1.3.1].

The design of ultrasound systems capable of operating with a wide range of transducers poses several problems. One key challenge is the impedance mismatch which commonly occurs because the impedance of different transducers can vary from less than  $50\Omega$  to  $10k\Omega$  [1.3.2], [1.3.3], while the impedance of the electronics is fixed. Mismatched impedances can seriously compromise the effectiveness of an ultrasound system, even if the transducer and electronics individually have outstanding performance. To maximize the efficiency with which the signal power is transferred requires a matching network, and a different network must be designed for each configuration.

Another challenge is that the electronics need to be designed appropriately for different types of transducers [1.3.3]. A transducer is driven by a high-voltage transmitter, which must generate a pulse with a shape that suits the impulse response of that transducer. The parameters of all the components in the front-end receiver, including the

gains of amplifiers, the bandwidths of filters, and the sampling-rate and resolution of the analog-to-digital converter (ADC) will be determined by the transducer's two-way impulse response.

Despite these interdependencies, the transducers and the electronics in an ultrasound system are commonly developed independently, making it difficult to optimize performance. This motivates our development of a pulse-echo ultrasound system simulator. Most previous studies [1.3.4]-[1.3.14] have only focused on the modeling of the transducer and ultrasound field as an equivalent electrical circuit. The modeling of transducers themselves [1.3.4]-[1.3.9] has largely been based on theoretical models, such as those of Mason [1.3.10], Redwood [1.3.11], KLM [1.3.12], and Leach [1.3.13]. These theoretical models, based on knowledge of the transducers' material properties and physical dimensions, are best suited to the optimization of a transducer during its design and manufacture.

Alternatively, an analytical model based on experimental measurements allows system designers to simulate transducers without reference to their physical specifications [1.3.14]. To combine a model of this sort with electronics within an analog circuit simulator requires the transducer model to be transformed to a lumped passive-circuit model. Moreover, system-level simulation using an analog simulator requires a time-consuming transistor-level design of the electronics; and these circuits still have to be redesigned to permit a full analysis of subsequent parameter changes.

A third possibility, which allows a system designer to investigate the behavior of a pulse-echo ultrasound system from a more complete electro-acoustic point of view, is to

simulate both the transducer and the electronics in the same high-level environment.

In this thesis, we present a simulator of this type, in which both the ultrasound components and the electronics of a pulse-echo ultrasound system are represented by a single Matlab/Simulink model.

This approach supports a two-way (transmit and receive) analysis of ultrasound system. Unlike other simulators [1.3.15]-[1.3.19], high-voltage pulse generation, electrical signal conditioning, and analog-to-digital conversion can be simulated with the transducer. Modeling the transducer as a transfer function, which can be derived from pulse-echo measurements made during manufacturing, makes it easy to change the transducer in the simulation. Moreover, by inserting transfer functions into the signal path to account for the impedances of both the transducer and the electronics, impedance mismatches can be analyzed and corrected.

Our simulator includes all the parameters that the designers of an ultrasound system require to specify the electronics. Thus the best pulse for a given transducer can be determined using the high-voltage transmitter model and, since the front-end receiver model is based on a specific architecture, the specifications of each component in the receiver can readily be determined. Finite element modeling (FEM) can also be considered to simulate the electronics. It is also a powerful tool but with complicated and time-consuming method [1.3.20]. On the other hand, our approach reduces the simulation time while keeping high accuracy and it is able to provide the microelectronics designers with affordable system-level feedback in a short time [1.3.21].

## **1.4 THESIS ORGANIZATION**

The thesis, organized into six chapters, describes the modeling methodology of a pulse-echo ultrasound system for medical imaging diagnostics.

The first chapter introduces the general description of ultrasound imaging with its history, challenge in the developments of ultrasound systems and our approach. Chapter 2 outlines the key points of ultrasound system fundamentals; basic ultrasound physics, the basics of piezoelectric transducers and ultrasound system overview. Chapter 3 describes Chapter 3 introduces literature review of ultrasound transducer modeling, which is the most important for the simulation of pulse-echo ultrasound systems. Chapter 4 the building blocks of the proposed simulator are presented and the MATLAB/Simulink implementation of the subsystems – high-voltage transmitter, acoustic subsystem, interfacing electronics, and front-end receiver – is described in detail. In chapter 5, we present the results of experiments designed to validate the accuracy of our simulator and discuss with these results. Chapter 6 summarized the achievements of this study and its possible impact on ultrasound imaging.

## CHAPTER 2

# FUNDAMENTALS OF ULTRASOUND SYSTEMS

### 2.1 BASIC ULTRASOUND PHYSICS

#### 2.1.1 SOUND WAVES

Sound is mechanical energy that is transmitted by pressure waves through a medium. Periodic changes in the pressure of the medium (air or water or iron) are created by forces acting on the molecules, causing them to oscillate about their normal, unperturbed positions. Since the motion of the molecules (particles) is repetitive, the term *cycle* is used to describe any sequence of changes in molecular motion (particle displacement, density of molecules, pressure, and particle velocity) that recurs at regular intervals.

The *frequency* of wave is the number of a wave is the number of vibrations (back and forth movements) that a molecule makes per second or the number of times the cycle is repeated each second. For comparative purposes, higher frequency means that the cyclic motion is executed at a faster rate and more cycles are completed in the 1-second interval than at lower frequency. Sound waves are those pressure changes that the human

ear can detect. They oscillate at frequencies of 20 to 20,000 cycles/second (1/s), also referred to as hertz (Hz).

Wavelength is the extent of one complete wave cycle. A cycle is a sequence of changes in amplitude that recur at regular intervals. When particle density is plotted against distance, amplitude describes the variation in density. Wavelength is the distance between two successive equivalent density zones and is expressed in unit of a meter (m), centimeter (cm), or millimeter (mm).

Amplitude is the change in magnitude of a physical entity. The term can be applied to pressure in the medium or to particle density, particle displacement, or particle velocity in the medium. It has other applications, such as to characterize the size of a voltage pulse delivered to or induced within the crystal of the transducer. When the amplitude is plotted as a function of time, the period of the wave is defined as the time necessary for one complete cycle or the time between two successive compression zones or rarefaction zones. Alternatively, the period is the elapsed time between compression zones as the sound wave passes through one point in the medium. The unit of the period is the second.

The frequency of a wave is the number of cycles occurring at a given point in one unit of time. It corresponds to the inverse of the period. The unit of frequency is the hertz, which is equal to 1 cycle per second. Cycle is not a standard of measurement but is used as a descriptor to clarify the concept of frequency. Often frequency is expressed in units of inverse time only.

The speed at which a wave propagates through the medium is called the acoustic velocity ( $c$ ). In physics, velocity is usually considered a vector quantity – magnitude and



direction are assigned. In ultrasound physics the term velocity traditionally refers to magnitude only. The velocity of sound is determined by the rate at which the wave energy is transmitted through the medium, which depends on the density and compressibility of the medium.

The velocity of sound or ultrasound remains constant for a particular medium. The velocity ( $c$ ) is equal to the frequency ( $f$ ) times the wavelength ( $\lambda$ ). Stated mathematically:

$$c = f \cdot \lambda, \quad (2.1.1)$$

This is probably the most important equation used in diagnostic ultrasound. Because the velocity is constant for a particular medium, increasing the frequency causes the wavelength to decrease.

### 2.1.2 REFLECTION

The major interaction of interest for diagnostic ultrasound is reflection. If a sound beam is directed at right angles (called normal incidence) to a smooth interface (e.g., the boundary between different tissue types) large than the width of the beam, it will be partially reflected toward the sound source as shown in Fig. 2.1.1. These interfaces, called specular reflectors, are responsible for the major organ outlines seen in diagnostic ultrasound examinations.

A difference in acoustic impedances causes some portion of the sound to be reflected at the interface. The product of density ( $\rho$ ) times velocity ( $c$ ) is called the acoustic impedance ( $Z$ ):

$$Z = \rho \cdot c, \quad (2.1.2)$$

This quantity is a measure of the resistance to sound passing through the medium. Acoustic impedance is expressed as kilograms per square meter per second ( $\text{kg/m}^2/\text{s}$ ). In the international system of units (SI) this combination of  $\text{kg/m}^2/\text{s}$  is given a special name, the rayl.

For perpendicular incidence, the reflection coefficient for intensity is expressed as follows:

$$\alpha_r = \left( \frac{Z_2 - Z_1}{Z_2 + Z_1} \right)^2, \quad (2.1.3)$$

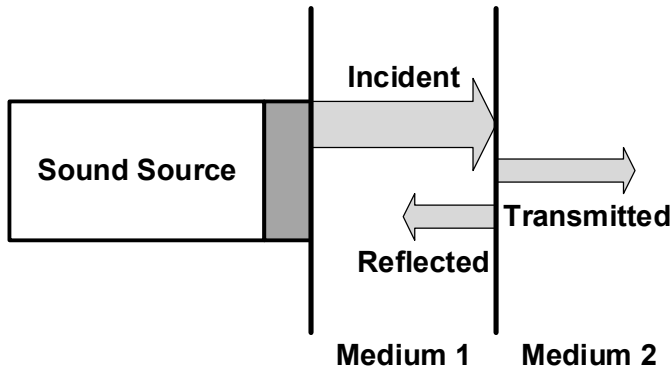


Fig. 2.1.1. Reflection caused by a sound wave striking a large smooth interface at normal incidence.

where,  $\alpha_r$  is the reflection coefficient,  $Z_2$  the acoustic impedance of medium number 2 and  $Z_1$  the acoustic impedance of medium number 1. The transmission coefficient ( $\alpha_t$ ) is calculated 1 minus the reflection coefficient.

$$\alpha_t = \frac{4Z_2 \cdot Z_1}{(Z_2 + Z_1)^2}, \quad (2.1.4)$$

It does not matter which impedance is the larger or smaller for two materials composing the interface - the difference between them squared gives the same number. Thus the same percentage of reflection occurs at the interfaces, whether sound is going from a high acoustic impedance to a low acoustic impedance, or vice versa. If the acoustic impedance difference is small, the magnitude of the reflected wave will be small.

Table 2.1.1 Acoustic impedance of some main biological tissues

<b>Material</b>	<b>Sound velocity (m/sec)</b>	<b>Acoustic impedance (<math>10^6 \text{ kg/m}^2 \text{ s}</math>)</b>
Water	1480	1.48
Air	330	0.0004
Blood	1570	1.61
Fat	1410-1470	1.34-1.39
Muscle	1590	1.71
Bone	4000	8.8
Soft tissue	1540	1.62

Because the same device transmits and receives the sound waves, maximum detection of the reflected echo occurs when the sound beam strikes the interface with normal incidence. If the acoustic impedance difference is large, such as in bone compared to soft tissue, a large fraction of sound will be reflected; of the transmitted beam will penetrate structures behind the bone, and much will return to the detector. Table 2.1.1 shows the acoustic impedance of some main biological tissues [2.1.1].

### 2.1.3 SCATTERING

Another important interaction between ultrasound and tissue is scattering, or nonspecular reflections, which is responsible for providing the internal texture of organs in the image. The scattering occurs because the interfaces are small, with physical dimensions approximately the size of the wavelength or smaller. Each interface acts as a new separate sound source, and sound is reflected in all directions independent of the direction of the incoming sound wave as shown in Fig. 2.1.2. The magnitude of scattered ultrasound intensity is much weaker than for specular reflection and depends on the number of scatterers per volume, size of the scatterers, acoustic impedance, and frequency.

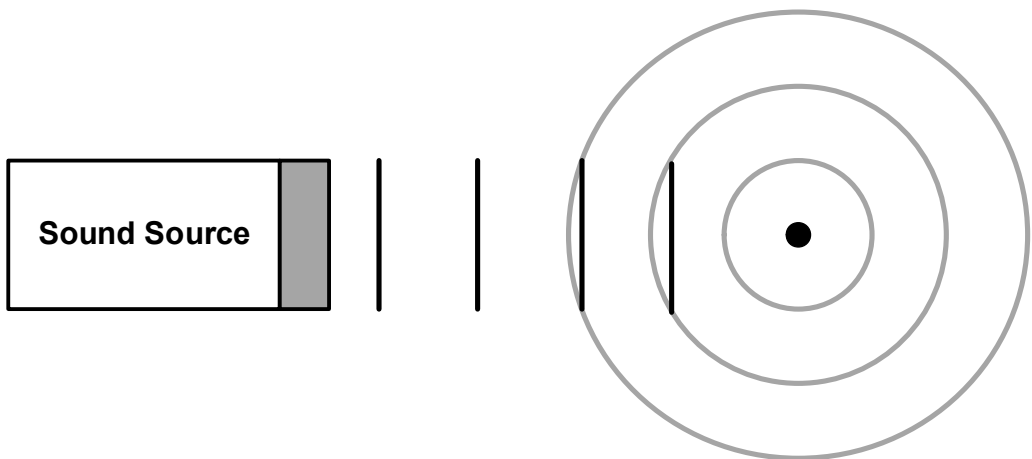


Fig. 2.1.2. Nonspecular reflection (scattering). The scattered wave from a small structure indicated in gray is emitted in all directions, shown here in two dimensions only.

#### 2.1.4 REFRACTION

Another interaction that occurs between ultrasound and tissue is refraction. If the ultrasound beam strikes an interface between two media at an angle of 90 degrees (normal incidence), a percentage will be reflected back to the first medium, and the rest will be transmitted into the second medium without a change in direction. If the beam strikes the interface at an angle other than 90 degrees, however, the transmitted part will be refracted or bent away from the straight-line path as shown in Fig. 2.1.3. Refraction of sound waves obeys Snell's law, which relates the angle of transmission to the relative velocities of sound in the two media. Snell's law is given by

$$\frac{c_i}{c_t} = \frac{\sin \theta_i}{\sin \theta_t}, \quad (2.1.5)$$

where  $\theta_i$  is the incident angle,  $\theta_t$  the transmitted angle,  $c_i$  the velocity of sound in the incident medium, and  $c_t$  the velocity of sound in the transmitted medium. In Snell's law the angle  $\theta_i$  and  $\theta_t$  are defined with respect to a line drawn perpendicular to the interface.

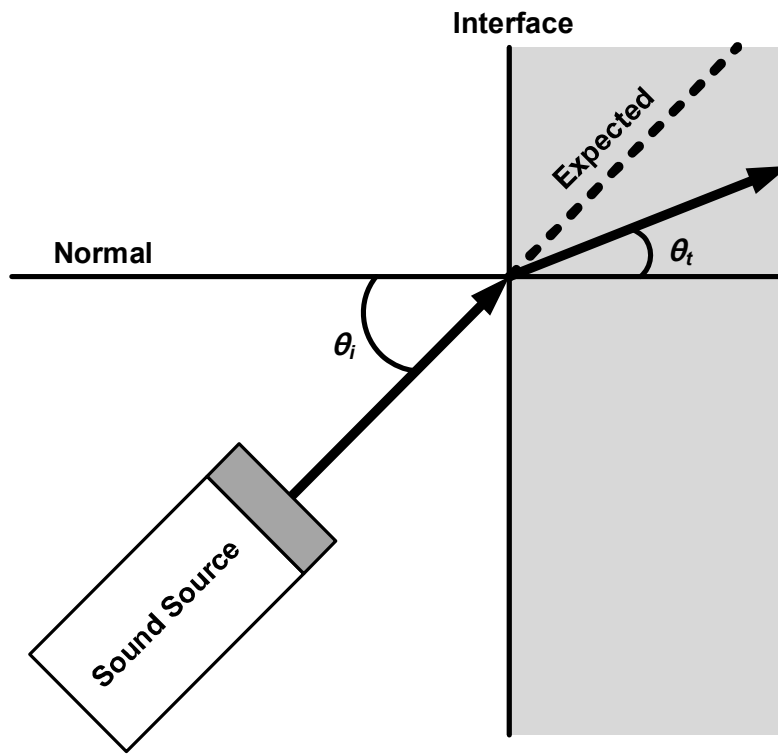


Fig. 2.1.3. Case of refraction. The velocity of a sound beam in the incident medium is less than that in the transmitted medium, causing the beam to be bent away from the normal.

### 2.1.5 DIFFRACTION

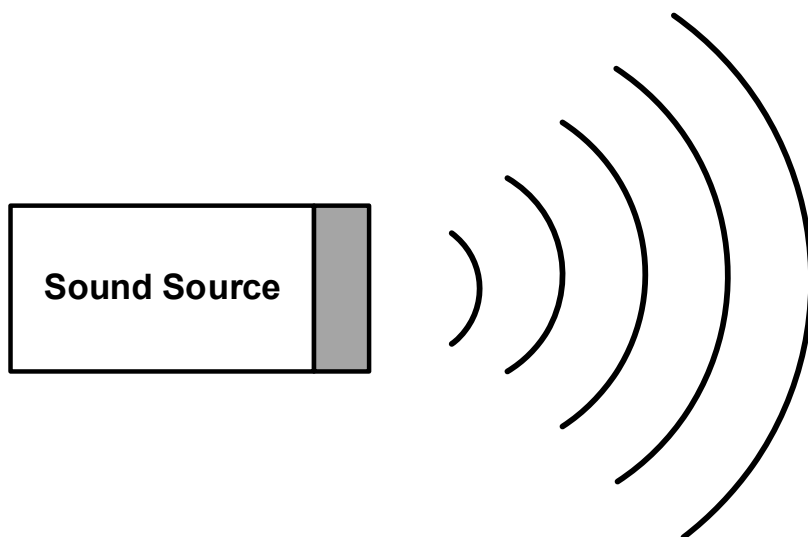


Fig. 2.1.4. Divergence of a sound beam from a small source.

Diffraction causes the ultrasound beam to diverge or spread out as the waves move farther from the sound source as shown in Fig. 2.1.4. The rate of divergence increases as the size (diameter) of the sound source decreases. Diffraction also occurs after the beam with planar wave-fronts passes through a small aperture on the order of one wavelength. Because the wave is blocked everywhere but in the area of the aperture, the aperture acts as a small sound source, and the beam diverges rapidly.



### **2.1.6 ABSORPTION**

Absorption is the only process whereby sound energy is dissipated in a medium. All other modes of interactions decrease the ultrasonic beam intensity by redirecting the energy of the beam. Absorption is the process whereby ultrasonic energy is transformed into other energy forms, primarily heat. It is responsible for the medical applications of therapeutic ultrasound.

The absorption of an ultrasound beam is related to the beam's frequency and to the viscosity and relaxation time of the medium. The relaxation time describes the rate at which molecules return to their original positions after being displaced by a force.

If a substance has a short relaxation time, the molecules return to their original positions before the next wave compression arrives. If a substance has a long relaxation time, however, the molecules may be moving back toward their original positions as the wave crest strikes them. More energy is required to stop and then reverse the direction of the molecules, and this produces more heat. The ability of molecules to move past one another characterizes the viscosity of a medium; high viscosity provides great resistance to molecular flow.

The frequency also affects absorption in relation to both the viscosity and the relaxation time. If the frequency is increased, the molecules must move more often, thereby generating more heat from the drag caused by friction. Also, as the frequency is increased, less time is available for the molecules to recover during the relaxation process. Molecules remain in motion, and more energy is necessary to stop and redirect them,

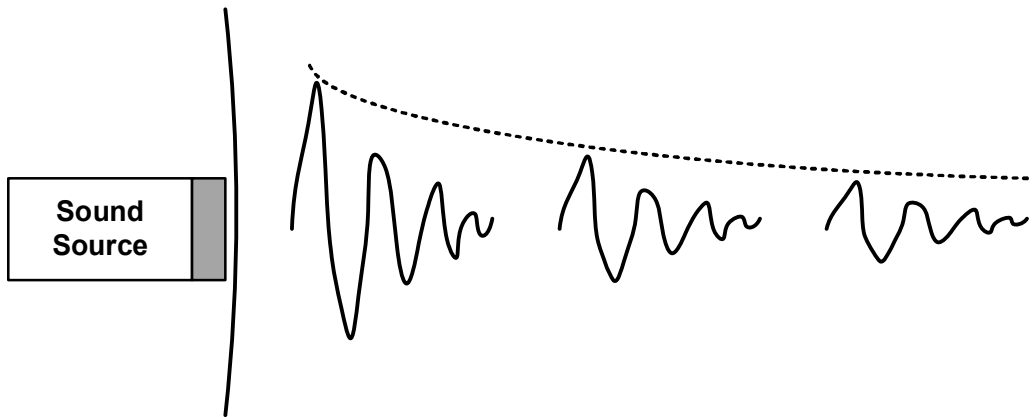


Fig. 2.1.5. Attenuation of acoustic pressure as a sound beam penetrates the medium.

again producing more absorption. The rate of absorption is directly related to the frequency. If the frequency doubles, the rate of absorption also doubles.

The peak amplitude of acoustic pressure (pascal), particle density ( $\text{kg/m}^3$ ), particle displacement (m), and particle velocity (m/s) all decrease as the wave traverses a homogeneous medium. Fig. 2.1.5 shows the absorption of the pulsed ultrasonic beam follows an exponential function as the pulsed wave penetrates the tissue. Absorption is enhanced if the frequency is increased.

### **2.1.7 ATTENUATION**

Attenuation includes the effects of both scattering and absorption in the characterization of amplitude reduction as the ultrasound wave propagates through a medium. Attenuation is also described by an exponential function dependent on the distance traveled, composition of the medium, and the frequency. As frequency is increased, the reduction of the ultrasound intensity with distance becomes more pronounced. This has a practical consequence in medical imaging. The ultrasound beam and returning echoes used to form the image must travel through tissue. The depth of penetration becomes less as frequency is increased – the ability to observe deep-lying structures is forfeited.

At a particular location within a continuous single-frequency ultrasonic field, the variations of pressure with time demonstrate an oscillatory behavior, the greatest deviations occurring during maximum pressure. The maximum particle velocity and the maximum particle displacement are related to the maximum pressure. As the maximum pressure is reduced, a corresponding decrease in particle velocity and particle displacement occurs.

Table 2.1.2 shows some intensity attenuation factors for human tissues at a frequency of 1MHz.

Table 2.1.2 Attenuation of human tissues and other media at 1MHz

<b>Material</b>	<b>Attenuation (dB/cm)</b>
Blood	0.18
Fat	0.6
Kidney	1
Muscle (across fibers)	3.3
Muscle (along fibers)	1.2
Brain	0.85
Liver	0.9
Lung	40
Skull	20
Lens	2
Aqueous humor	0.022
Vitreous humor	0.13
Water	0.0022
Castor oil	0.95

## 2.2 ULTRASOUND SYSTEM OVERVIEW

Fig. 2.2.1 shows a simplified diagram of an ultrasound system [2.1.1]. In most systems the transducer element is connected to the end of a relatively long cable of about 2 m. In traditional ultrasound, this cable has from a minimum of 48 and up to 256 micro-coaxial cables, and is usually one of the most expensive parts of the system. For 3-D ultrasound, the number of channels increases dramatically, and the number of cables can typically not be correspondingly large. In traditional systems the transducer elements directly drive the cable, which can result in significant signal loss due to the loading of the cable capacitance on the transducer elements. Unfortunately, this in turn demands that the receiver noise figure (NF) is lower by the amount of the cable loss. The loss is typically on the order of 1-3 dB depending on transducer and operating frequency. In most systems multiple probe heads can be connected to the system, this allows the operator to select the appropriate transducer for optimal imaging. The heads are selected via High Voltage (HV) relays; these relays introduce a large parasitic capacitance in addition to the cable.

A high-voltage mux/demux is used in some arrays to reduce the complexity of transmit and receive hardware at the expense of flexibility. The most flexible systems are phased array digital beamforming systems where all transducer elements can be individually phase and amplitude controlled. These also tend to be the most expensive systems due to the need for full electronic control of all channels.

On the transmit side the TX beamformer determines the delay pattern and pulse train

that set the desired transmit focal point. The outputs of the beamformer are then amplified

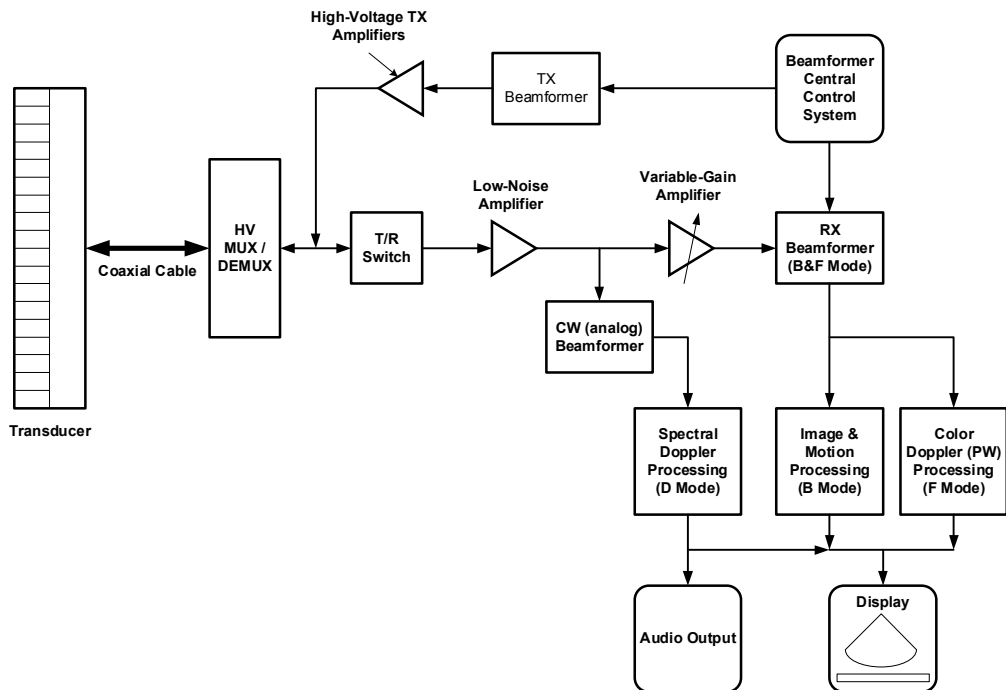


Fig. 2.2.1 Ultrasound system block diagram.

by high voltage transmit amplifiers that drive the transducers. These amplifiers might be controlled by DACs to shape the transmit pulses for better energy delivery to the transducer elements. Typically multiple transmit focal regions (zones) are used, i.e. the field to be imaged is divided up by focusing the transmit energy at progressively deeper points in the body. The main reason for doing this is to increase the transmit energy for points that are deeper in the body because the signal is heavily attenuated as it travels into the body.

On the receive side there is a transmit/receive switch, generally a diode bridge,

which blocks the high transmit voltage pulses, followed by a low noise amplifier and variable gain amplifiers which implement the time gain compensation and sometimes also apodization functions; spatial windowing to reduce side lobes in beam. Time-gain control (TGC) is under operator control and used to maintain image uniformity. After amplification, beamforming is performed which can be implemented in analog (ABF) or digital (DBF) form. Digital beamforming is usually preferred in modern systems except for continuous wave (CW) Doppler processing whose dynamic range is mostly too large to be processed through the same channel as the image. Finally, the Rx beams are processed to show either a gray scale image, color flow overlay on the 2-D image, and/or a Doppler output.

## **2.3     PIEZOELECTRIC TRANSDUCER**

The fundamental working principle of a piezoelectric ultrasound transducer is based on the piezoelectric effect. When a mechanical force in the form of an ultrasound wave is applied to a transducer, along with geometric deformation, polarization of the electrical dipoles in the transducer dielectric occurs. Thus, a net dipole moment is created, which forms an electric field across the two electrodes of the transducer [2.3.1]. The polarization is proportional to the mechanical force, and changes sign depending on the sign of the pressure wave [2.3.2]. Inversely, if an ultrasound transducer is excited with alternating electric fields, it will compress and expand, and thereby generating sound waves in the ultrasonic range.

Many crystalline materials can be used to build piezoelectric ultrasound transducers, which can be categorized as natural crystals (e.g. quartz, Rochelle salt) or man-made ceramics (e.g. barium-titanate ceramics, leadzirconate-titanate ceramics). Among them, the lead-zirconate-titanate ceramic, known as PZT, is the most widely used material [2.3.3]. It is also the building material for transducers used in this thesis project. It is worth noting that the piezoelectric property of a PZT ultrasound transducer will be lost if the temperature of the crystal rises above its Curie temperature. The temperature requirement puts constraints on the transducer-to-chip interconnection technology. Therefore, we should keep the processing temperature well below the Curie temperature of the selected PZT ceramic.

A typical piezoelectric ultrasound transducer is a layered device consisting of two



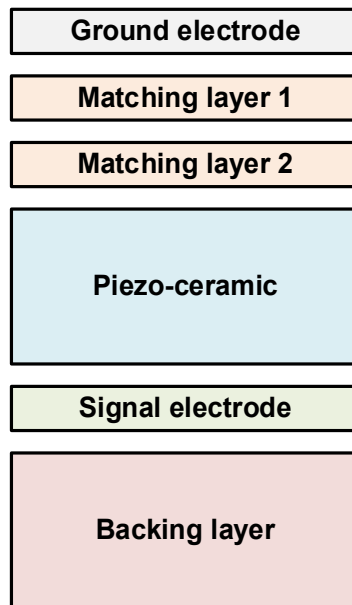


Fig. 2.3.1 Structure of a typical piezoelectric transducer.

electrodes, a piece of piezo-ceramic, a backing layer and one or more matching layers as shown in Fig. 2.3.1. The electrodes should be sufficiently thin so that their influence on wave propagation is negligible [2.3.2]. The piezo-ceramic is the actual ultrasound generator and detector, which is sandwiched between the signal electrode and the ground electrode. The size and shape of the piezo-ceramic determine the resonance frequency of the transducer, at which the energy-conversion efficiency of the transducer reaches its highest value [2.3.4]. The frequency response of a piezoelectric ultrasound transducer has a band-pass shape. The bandwidth determines the range of frequencies over which the transducer can operate with relatively high energy conversion efficiency.

Since the acoustic impedances between the piezo-ceramic and the tissue being

imaged differ greatly (e.g. the acoustic impedance of PZT ceramic is about 20-30 times higher than that of soft tissue [2.3.5]), connecting the piezoceramic directly to the tissue would cause strong reflection at the boundary. In this case, in the transmit mode, only a small percentage of the acoustic energy would then be transmitted into the tissue. The reflected waves would cause unwanted ringing of the piezo-ceramic, which would degrade the axial resolution discussed in Section 2.1.4 of the image due to very long pulse duration. Moreover, in the receive mode, large reflection would result in a low sensitivity.

To improve the energy transfer efficiency at the transduce-tissue boundary and enhance the sensitivity, one or more matching layers are employed. Matching layers have acoustic impedance levels between those of the piezoceramic and the tissue. The use of matching layers allows the sound waves to reflect back and forth repeatedly inside the matching layers, producing waves that are in phase to each other. Hence, waves are constructively added up to form a reinforced wave that propagates across the boundary. In this way, the sensitivity of the transducer is improved. In addition to the aforementioned advantage, as described in [2.3.5], by using several matching layers to gradually bridge the gap of acoustic impedances between the tissue and the piezo-ceramic, the bandwidth of the transducer can be tuned. In the meantime, to overcome the ringing problem, a backing layer is attached underneath the piezo-ceramic, so that during transmission, most of the energy reflected back into the piezo-ceramic can be absorbed and turned into heat. The backing layer also provides damping to the received echo signals. The durations of the echoes are as well shortened for better axial resolution.

## **2.4 HIGH-VOLTAGE TRANSMITTER**

A digital transmit beamformer typically generates the necessary digital transmit signals with the proper timing and phase to produce a focused transmit signal. High-performance ultrasound systems will generate complex transmit waveforms using an arbitrary waveform generator to optimize image quality. In these cases, the transmit beamformer generates digital 8-bit to 10-bit words at rates of approximately 40MHz to produce the required transmit waveform. Digital-to-analog converters (DACs) are used to translate the digital waveform to an analog signal, which is then amplified by a linear high-voltage amplifier to drive the transducer elements. This transmit technique is generally reserved for more expensive and less portable systems, as it can be very large, costly, and power hungry. As a result, the majority of ultrasound systems do not use this transmit-beamformer technique, but instead use multilevel high-voltage pulsers to generate the necessary transmit signals. In this alternate implementation highly-integrated, high-voltage pulsers quickly switch the transducer element to the appropriate programmable high-voltage supplies to generate the transmit waveform. To generate a simple bipolar transmit waveform, a transmit pulser alternately connects the element to a positive and negative transmit supply voltage controlled by the digital beamformer. More complex realizations allow connections to multiple supplies and ground in order to generate more complex multilevel waveforms with better characteristics.

## **2.5 FRONT-END RECEIVER**

A T/R switch protects the LNA from the high-voltage transmit pulse and isolates the LNA's input from the transmitter during the receive interval. The switch is usually implemented using an array of properly biased diodes which automatically turn on and off when presented with a high-voltage transmit pulse. The T/R switch must have fast recovery times to ensure that the receiver is on immediately after a transmit pulse. These fast recovery times are critical for imaging at shallow depths and for providing a low on-impedance to ensure that receiver noise sensitivity is maintained.

The LNA in the receiver must have excellent noise performance and sufficient gain. In a properly designed receiver the LNA will generally determine the noise performance of the full receiver. The transducer element is connected to the LNA through a relatively long coaxial transducer cable terminated into relatively low impedance at the LNA's input. Without proper termination the cable capacitance, combined with the transducer element's source impedance, can significantly limit the bandwidth of the received signal from a broadband transducer. Termination of the transducer cable into a low impedance reduces this filtering effect and significantly improves image quality. Unfortunately, this termination also reduces the signal level at the input to the LNA and, therefore, tends to reduce the receiver's sensitivity. Consequently, it is important for the LNA to have active-input-termination capability to provide the requisite low-input impedance termination and excellent noise performance required under these conditions.

The VGA, sometimes called a time gain control (TGC) amplifier, provides the

receiver with sufficient dynamic range over the full receive cycle. Ultrasound signals propagate in the body at approximately 1540m/sec and attenuate at a rate of about 1.4dB/cm-MHz roundtrip. Immediately after an acoustic transmit pulse, the received "echo" signal at the LNA's input can be as large as  $0.5V_{p-p}$ . This signal quickly decays to the thermal noise floor of the transducer element. The dynamic range required to receive this signal is approximately 100dB to 110dB, and is well beyond the range of a realistic ADC. As a result, a VGA is used to map this signal into the ADC. A VGA with approximately 30dB to 40dB of gain is necessary to map the received signal into a typical 12-bit ADC used in this application. The gain is ramped as a function of time (i.e., "time gain control") to accomplish this dynamic range mapping.

The AAF in the receive chain keeps high-frequency noise and extraneous signals that are beyond the normal maximum imaging frequencies from being aliased back to baseband by the ADC. Many times an adjustable AAF is provided in the design. To avoid aliasing and to preserve the time-domain response of the signal, the filter itself needs to attenuate signals beyond the first Nyquist zone.

The ADC used in this application is typically a 12-bit device running from 40Msps to 60Msps. This converter provides the necessary instantaneous dynamic range at acceptable cost and power levels. In a properly designed receiver, this ADC should limit the instantaneous SNR of the receiver. As previously mentioned, however, limitations in the poor-performing VGAs many times limit receiver SNR performance.

## **CHAPTER3**

# **MODELING OF ULTRASOUND TRANSDUCER**

### **3.1 THEORETICAL MODELS**

#### **3.1.1 LEACH MODEL**

Modeling a pulse–echo ultrasound system is very challenging because of the ultrasound transducer which involves both electrical and mechanical properties. The transducer has been successfully modeled using equivalent circuits such as Mason [3.1.1], Redwood [3.1.2], and the KLM model proposed by Krimholtz et al. [3.1.3]. Many research have been carried out to implement these equivalent circuits on a computer-aided design (CAD) tool such as SPICE [3.1.4]–[3.1.7]. In contrast to the finite element method (FEM) which calculates direct resolution of the piezoelectric equations using numerical methods, this simulation method can easily be adapted to any configuration provided that we have the suitable equivalent circuit; thus, it offers much more flexibility.

The previous models [3.1.1]–[3.1.3] have some weakness. The transformer primary–secondary ratio varies according to the frequency and it is difficult to make its implementation on a simulation environment. Also, the negative capacitance

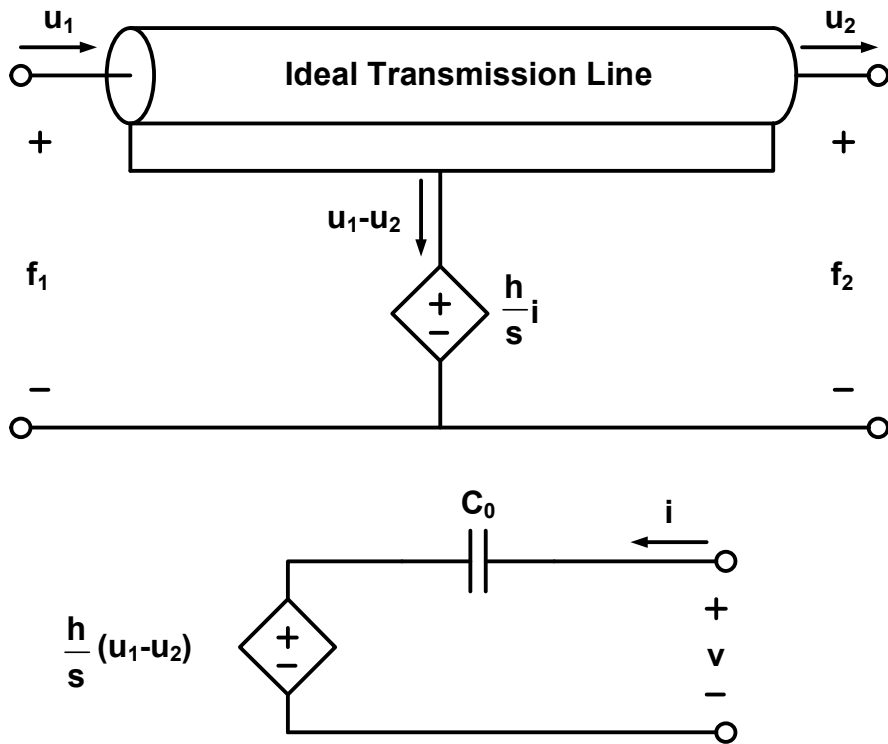


Fig. 3.1.1 Leach model, analog circuit for the thickness-mode transducer

does not physically make sense. Unlike those models, the Leach model [3.1.8] proposed a smart way to avoid these weakness by using controlled sources to express the energy transformation between the electrical and acoustical port. The SPICE implementation of the Leach model is shown in Fig. 3.1.1. The electrical port of the transducer is represented by the couple voltage–current  $(v, i)$ , whereas the acoustical ports are modeled by the couple force–particle velocity  $(f_1, u_1)$  for backing material and the couple  $(f_2, u_2)$  for the propagating medium.

The Leach model parameters are calculated from the electrical and acoustical

characteristics of the transducer according to the following equations:

The piezoelectric field constant (in newtons per coulomb)

$$h = \frac{e}{\varepsilon^s} \quad (3.1.1)$$

where  $e$  is the piezoelectric constant (in coulombs per square meter), and  $\varepsilon^s$  is the relative permittivity at constant deformation.

The static capacitance of the transducer (in farads)

$$C_0 = \frac{\varepsilon^s A}{\delta} \quad (3.1.2)$$

where  $A$  is the cross section of the transducer, and  $\delta$  is its thickness.



### 3.1.2 ACOUSTICAL ATTENUATION

Losses in piezoelectric material are of two different causes: dielectric and mechanical loss. Dielectric losses can be modeled by change of the electrical part of the equivalent circuit. Mechanical losses can be modeled by change of the transmission line, which is the mechanical part of the equivalent circuit. Lossy transmission lines can be modeled as lumped ladders consisting of the elements  $L'$ ,  $R'$ ,  $C'$ ,  $G'$  per unit of length  $dl$  as shown Fig. 3.1.2.

The propagation of sinusoidal waves travelling along such a transmission line can be described with two complex quantities, the characteristic impedance  $Z_0$  and the propagation function  $\gamma$  [3.1.9]:

$$Z_0 = \sqrt{\frac{R' + j\omega L'}{G' + j\omega C'}} \quad (3.1.3)$$

$$\gamma = \alpha + j\beta = \sqrt{(R' + j\omega L')(G' + j\omega C')} \quad (3.1.4)$$

with  $j = \sqrt{-1}$  and  $\omega = 2\pi f$ . The real part of  $\gamma$  is the attenuation coefficient  $\alpha$  of the transmission line; the complex part  $\beta$  is a value for the phase velocity  $v_p$ :

$$v_p = \frac{\omega}{\beta}. \quad (3.1.5)$$

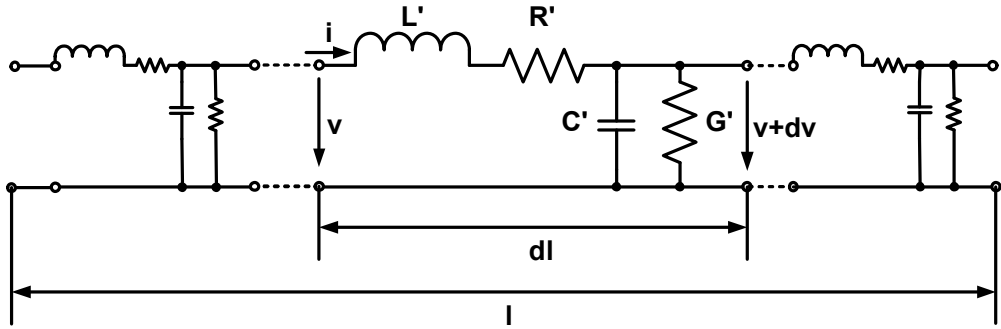


Fig. 3.1.2 Lumped segment of the lossy transmission line.

Assuming  $G'=0$  and  $R' \ll \omega L'$  (high frequencies), (3.1.3) and (3.1.4) can be approximated as follows:

$$Z_0 \approx \sqrt{\frac{L'}{C'}} \quad (3.1.6)$$

$$\gamma \approx \frac{R'}{2} \sqrt{\frac{C'}{L'}} + j\omega \sqrt{L'C'} \quad (3.1.7)$$

Thus the phase velocity is

$$v_p = \frac{1}{\sqrt{L'C'}}, \quad (3.1.8)$$

and the attenuation coefficient in nepers per unit of length is found to be

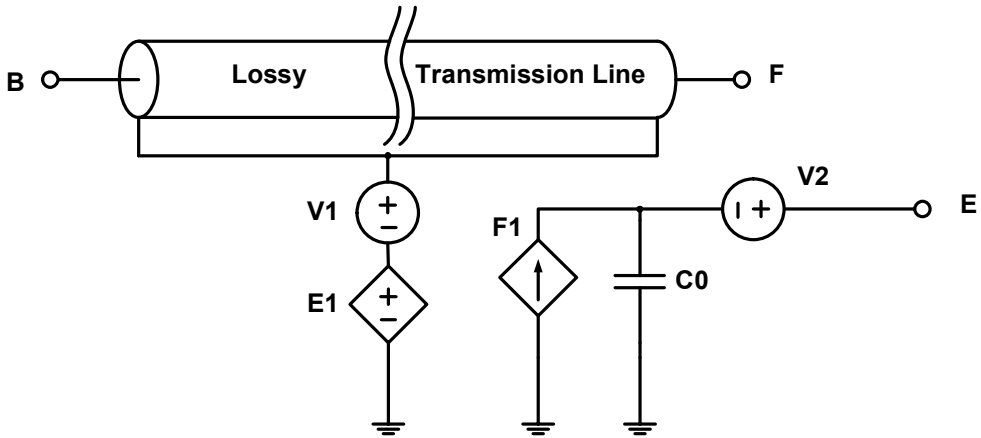


Fig. 3.1.3 Spice model of the lossy thickness-mode transducer.

$$\alpha \approx \frac{R'}{2} \sqrt{\frac{C'}{L'}}. \quad (3.1.9)$$

(3.1.8) and (3.1.9) may be rearranged as

$$\alpha \approx \frac{\omega}{2v_p} \cdot \frac{R'}{\omega L'} = \frac{\omega}{2v_p} \delta. \quad (3.1.10)$$

With the loss factor  $\delta = 1/Q$ , the same dependence is derived in [3.1.10] for acoustic losses in solid materials. For solids without scattering,  $Q$  is assumed to be constant and thus increases in proportion to frequency.

Fig. 3.1.3 shows the lumped model of the lossy thickness-mode transducer. The

PSpice internal model of the lossy transmission line is a distributed model with the parameters  $L'$ ,  $R'$ ,  $C'$ ,  $G'$  and length  $l$ .  $T_l$  is the lossy transmission line and the parameters of  $T_l$  are given by rearranging (3.1.6) and (3.1.8) to (3.1.10):

$$L' = \sqrt{\frac{Z_0}{v_p}}, \quad C' = \frac{1}{v_p \cdot Z_0}, \quad R = \frac{L'}{Q}, \quad G' = 0 \quad (3.1.11)$$

with the characteristic impedance  $Z_0 = A\rho v_p$ , where  $\rho$  is the density and  $v_p$  is the sound velocity of the transducer material. The parameter  $l$  is the thickness of the transducer.

### 3.1.3 PROPAGATING MEDIUM

The propagation medium is also can be modeled as electrical transmission lines when the ultrasound system is simulated with equivalent circuits [3.1.11]. The attenuation constant for an electrical transmission line can be written under the assumption of low-loss conditions ( $R \ll \omega L$ ,  $G \ll \omega C$ ):

$$\alpha = \frac{1}{2} \sqrt{LC} \left( \frac{R}{L} \right) + \frac{1}{2} \sqrt{LC} \left( \frac{G}{C} \right), \quad (3.1.12)$$

where  $R$  is resistance,  $G$  is conductance,  $C$  is capacitance, and  $L$  is inductance per unit length of the transmission line. This can be rewritten:

$$\alpha = \frac{1}{2} \frac{R}{Z_0} + \frac{1}{2} G Z_0, \quad (3.1.13)$$

where  $Z_0 = \sqrt{L/C}$  is the characteristic impedance of the transmission line.

A propagating sound wave is modeled as a forward travelling voltage wave in the transmission line. The amplitude of this voltage wave can be expressed as [3.1.12]:

$$|V(z)| = |V_0| e^{-\alpha z}, \quad (3.1.14)$$

where  $V_0$  is the voltage amplitude at  $z=0$ . (3.1.13) then gives:

$$|V(z)| = |V_0| e^{-(R/2Z_0)z} e^{-(GZ_0/2)}. \quad (3.1.15)$$

We can assign the following relationships to the lossy transmission line:

$$L = A\rho, \quad C = \frac{1}{A\rho c^2}, \quad R = 2\rho c A\alpha_v, \quad G = \frac{2}{\rho c A}\alpha_{tc} \quad (3.1.16)$$

where  $A$  is the cross-sectional area of the acoustic beam,  $\rho$  is the medium's density ( $\text{kg/m}^3$ ),  $\alpha_v$  is the coefficient of attenuation due to viscous losses, and  $\alpha_{tc}$  is the coefficient of attenuation due to thermal conduction. When the loss due to thermal conduction is negligible, the conductance  $G$  can be 0.

### 3.1.4 DIFFRACTION EFFECTS

Diffraction loss (i.e., beam spreading) is a major loss origin in low-loss media such as water. Considering the diffraction effect, an attenuation term is not dependent of the attenuation caused by  $R$ . This diffraction loss can be modeled by setting  $G \neq 0$ . In the [3.1.13], this is used to model the loss due to diffraction as:

$$A_{diff} = \frac{|V(z)|}{|V_0| e^{-(R/2Z_0)z}} = e^{-(GZ_0/2)}. \quad (3.1.17)$$

Solving for  $G$  gives:

$$G = \frac{2}{Z_0 z} \ln(A_{diff}), \quad (3.1.18)$$

which can be used as a parameter for the lossy transmission line, if the diffraction loss  $A_{diff}$  is known.

### 3.1.5 PARASITIC COMPONENTS

Parasitic components are unwanted resistance, inductance, and capacitance existing in cable, bond wires, and circuit board paths. To model the behavior of an electrical circuit accurately, these components might need to be considered. To be able to include the parasitics in a simulation, the values of the components need to be estimated. On chip level, this can be done by the parasitic extraction results of the layout tool. The same method can be applied for circuit boards. For bond wires that connect a chip to a socket approximate values can be achieved from the packaging facility.

Chip level capacitance and interconnect inductance are often in the nH and pF range as shown in Fig. 3.1.4. A coaxial cable that is used to connect the ultrasound machine with the transducer presents capacitance and inductance values that are considerably higher. Therefore, this often will be a dominating source of parasitic inductance and capacitance in the system.

A phenomenological explanation to the effects of the parasitic components arising in a coaxial cable, however, is easier to give if the lumped model is applied. [3.1.13] gives the lumped model of a coaxial cable. If the length of a coaxial cable is short compared to the wavelength of the propagating electromagnetic (EM) wave, the coaxial cable behaves as a lumped components consisting of a series inductor  $L_L$  (H) and a parallel capacitance  $C_L$  (F). The limit for when to use a lumped model is often drawn when the length of the conductor exceeds  $\lambda/10$ , where  $\lambda$  is the wavelength of the EM wave.



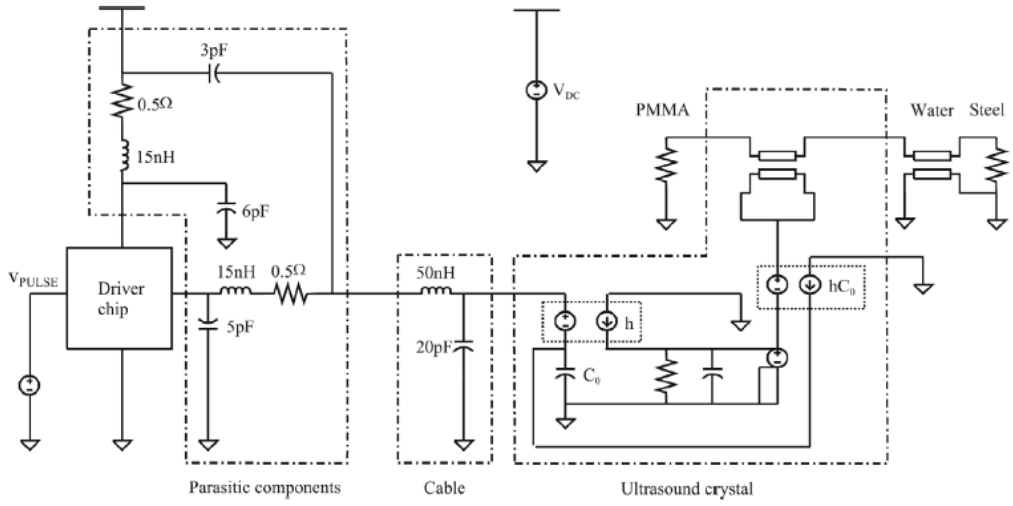


Fig. 3.1.4 Schematic used for simulation of parasitic components.

With a wavelength of:

$$\lambda = \frac{c}{f}, \quad (3.1.19)$$

the approximate upper frequency limit for when to use a lumped approach can be written:

$$f_{\text{lim}} = \frac{c}{10l}. \quad (3.1.20)$$

## 3.2 BUTTERWORTH VAN-DYKE MODEL

The Butterworth-Van Dyke (BVD) model can be derived from the measured impedance or admittance of the transducer. Therefore this model does not require the knowledge of the transducer's physical details. The transducer can be regarded as a one port electrical device so the impedance can be measured as shown Fig. 3.2.1.

The new modified BVD model has been presented to be covered for and high frequency ultrasonic transducers [3.2.1]. The schematic diagrams of conventional and modified BVD models are shown in Fig. 3.2.2.

The real resistance ( $R_1^*$ ) can be calculated from the magnitude of the resistance ( $R_1$ ) and phase angle ( $\theta_r$ ) at resonant frequency ( $\omega_r$ ). The inductance ( $L_1$ ) can be obtained at the resonant condition if we assume the magnitude of the impedance value at the resonant frequency is constant [3.2.2].

$$R_1^* = R_1 \cdot \cos(\theta_r), \quad (3.2.1)$$

$$L_1 = \frac{1}{\omega_r^2 C_1}, \quad (3.2.2)$$

The bulk capacitance ( $C_0$ ) can be calculated by the mechanical property or by the resonant condition.

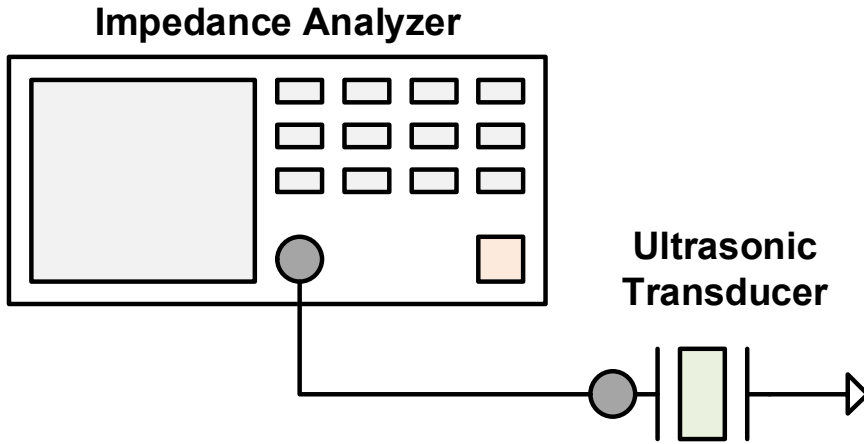


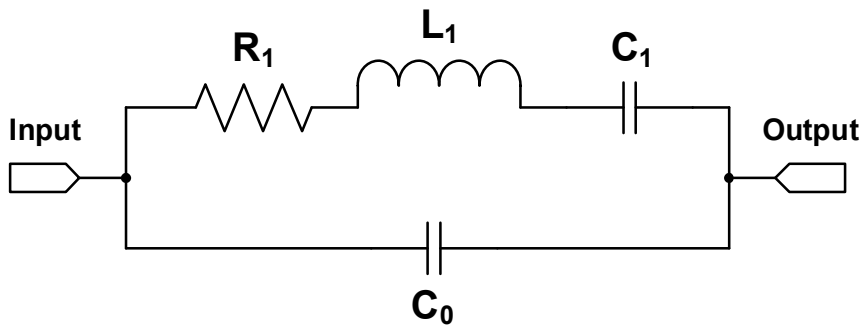
Fig. 3.2.1. Impedance measurement setup for ultrasound transducer.

$$C_0 = \frac{\left| \frac{X_r}{\sqrt{R_r^2 + X_r^2}} \right|}{\omega_r} \quad \text{or} \quad C_0 = \epsilon_0 \epsilon_r \frac{A}{d} \quad (3.2.3)$$

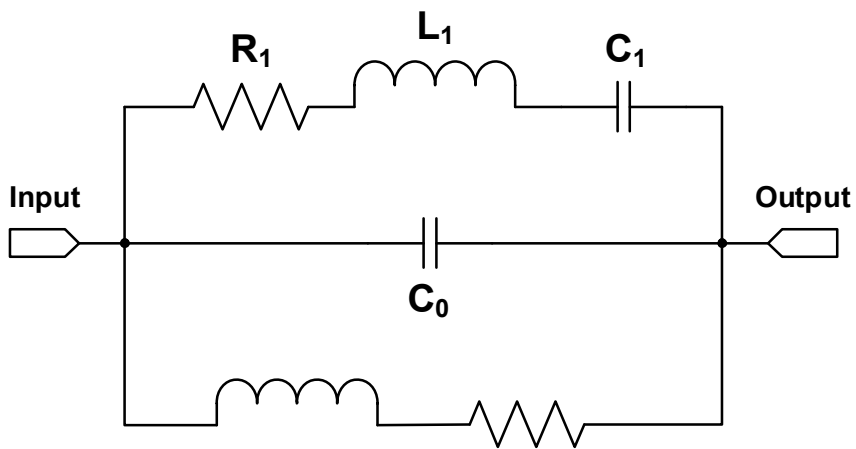
where  $C_0$  is the clamped capacitance,  $R_r$  and  $X_r$  are the resistance and admittance at resonant frequency,  $\epsilon_0$  and  $\epsilon_r$  are the dielectric constant at free space and a piezoelectric material,  $A$  and  $d$  are the surface and thickness of the material.

The capacitance  $C_1$  can be derived from the relationship between the resonant ( $\omega_r$ ) and anti-resonant frequency ( $\omega_a$ ).

$$C_1 = \left| C_0 \cdot \left( \left( \frac{\omega_a}{\omega_r} \right)^2 - 1 \right) \right| \quad (3.2.4)$$



(a)



(b)

Fig. 3.2.2. The schematic diagrams of (a) conventional and (b) modified BVD models.

The transformed clamped capacitance ( $C_0^*$ ) was re-defined according to the resonant and anti-resonant frequencies using the characteristic capacitances of the ultrasonic transducers.

$$C_0^* = C_0 - \frac{C_1 // C_0}{2Q_a} \quad (\text{if } Q_a \text{ is high}), \quad (3.2.5)$$

$$C_0^* = C_0 + \frac{C_1 // C_0}{2Q_a} \quad (\text{if } Q_a \text{ is low}) \quad (3.2.6)$$

where  $Q_a$  is the quality factor at anti-resonant frequency.

The impedance could be changed according to propagation medium. Thus, the radiation resistances ( $R_a$  and  $R_r$ ) were added to the model. These resistances could be obtained from the mechanical data.

$$R_r = \frac{\pi(Z_1 + Z_2)}{4k_t^2 \omega_r C_0 Z_C} \quad (3.2.7)$$

$$R_a = \left| \frac{4k_t^2 Z_C}{C_0(Z_1 + Z_2)} \right|^3 \frac{C_0^2}{\omega_a} \quad (3.2.8)$$

where  $Z_1$  and  $Z_2$  are the acoustic impedances at front and back port,  $k_t$  is the coupling factor,  $Z_C$  is the acoustic transducer impedance.

The inductance ( $L_2$ ) can be derived by the anti-resonant condition. The real resistance ( $R_2^*$ ) can be calculated by the magnitude of the resistance ( $R_2$ ) and phase angle ( $\theta_a$ ) at an anti-resonant frequency.

$$L_2 = \frac{R_2 \cdot Q_a}{\omega_a} \quad (3.2.9)$$

$$R_2^* = R_2 \cdot \cos(\theta_a) \quad (3.2.10)$$

where  $R_2$  is the resistance at anti-resonant frequency and  $\theta_a$  is the phase angle of the impedance at anti-resonant frequency. The real resistance ( $R_a^*$ ) at anti-resonant frequency can be calculated by

$$R_a^* = R_a \left[ 1 + Q_a^2 \right] \quad (3.2.10)$$

The loss term ( $R_L$ ) could be negligible. The modified BVD model could be constructed depending on the internal quality factors ( $Q_r$  and  $Q_a$ ) at the resonant and anti-resonant frequency. Thus, one more inductor ( $L_2$ ) and additional loss term ( $R_a^* // R_2^* // R_L$ ) were added and the clamped capacitance ( $C_0$ ) was also changed accordingly.

### 3.3 ANALYTICAL MODEL

The last methodology of the transducer modeling introduced in this thesis is the analytical model [3.3.1]. This model is developed starting from the experimental measurements of the driving point impedance and the electroacoustic transfer function of the ultrasound transducer. The model is gradually developed by using the data obtained from the pulse-echo measurements of a two-port black box.

The model is identified by two characteristic functions,  $Z(s)$  and  $W(s)$  in the Laplace domain, fitting the corresponding experimental curves. The identification procedure consists of two complementary phases. The first step determines the number, the type and the approximate position of poles and zeros. The second phase starts with the results obtained from the first one and reduces the mean-square-error of the fitting functions, by a modified version of the “simplex” optimization method [3.3.2], [3.3.3]. The optimization modifies the model parameter until the predefined model accuracy is achieved.

The model shown in Fig. 3.3.1 considers the ultrasonic system as a two-port black box. The input port is represented by the connector of the transducer. The input port is characterized by the driving point voltage  $V_s$  and current  $I_s$ . The output port provides a voltage  $V_h$ , corresponding to the transmitted acoustic axial field measured with a calibrated hydrophone. This analytical model is used here to predict transmitting characteristics of the transducer. Nevertheless the same modelling technique is suitable to devise a transducer model in receiving mode, where the output voltage of the

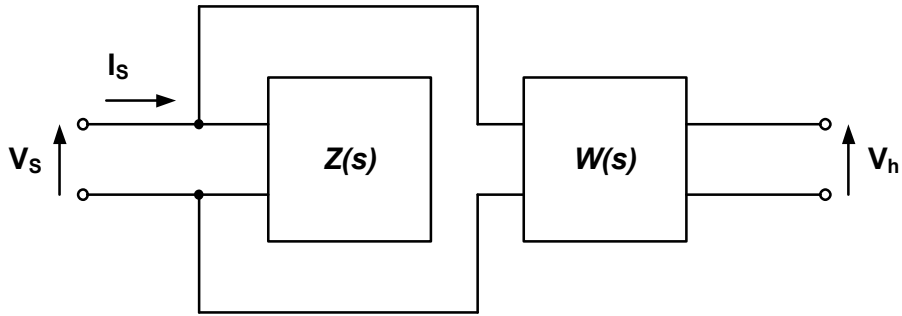


Fig. 3.3.1. The analytical model of the ultrasound transducer.

transducer is related to the incident field on the active surface.

Fig. 3.3.1 shows the model consisting of the input port function  $Z(s)$ , which represents the driving point impedance of the transducer and the voltage transfer function  $W(s)$ , both in the Laplace domain. With the assumption that the input impedance of the block  $W(s)$  is infinite, the driving point impedance is determined only by  $Z(s)$ .  $W(s)$  also represents the electroacoustic transfer function of the ultrasonic system. The  $W(s)$  function includes a propagation delay term  $\tau$ , introduced by the transducer itself and the measurement chain.

The actual driving point impedance and transfer function used as reference, are obtained from the time domain signals acquired with the experimental setup shown in Fig. 3.3.2. The immersion transducer is driven by a one cycle sinusoid at the transducers' nominal central frequency. The excitation signal generated at the output of the signal generator. Then, it is amplified by the power amplifier, which is needed to drive the probe under test. A one cycle sinusoid excitation signal has been chosen since the signal spectrum can be centered on the bandwidth of the transducer.



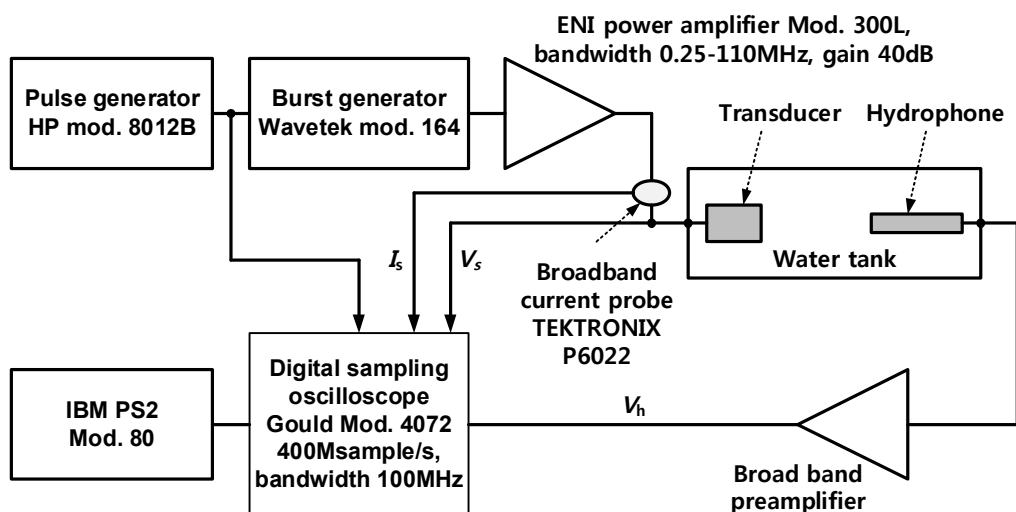


Fig. 3.3.2. Block diagram of the experimental setup.

The driving point voltage  $V_s$  and current  $I_s$  are sensed with a voltage probe and a broadband current probe. The ultrasonic axial far field distribution is measured by an 1-mm diameter PVDF hydrophone. The hydrophone spectral response is broad enough for the frequency range used in our measurement system. The hydrophone was placed in the transducer's far field. This condition reduces phase cancellation problems due to finite size of the hydrophone [3.3.4]. The hydrophone was aligned with the acoustic axis of the transducer and the output amplified with a wide bandwidth linear amplifier. For these measurements it was essential to use a broadband linear amplifier. In this paper, transimpedance amplifier is used with a linear phase response in the bandwidth 0-190MHz and phase deviation of  $1.2^\circ$ . Only a fraction of the bandwidth was required. The output voltage  $V_h$  was digitized and stored for an offline processing. This experimental

setup serves to calculate two reference curves for the approximation of  $Z(s)$  and  $W(s)$ , namely  $Z_M(j\omega_k)$  and  $W_M(j\omega_k)$  and obtained by the Fast Fourier Transform (FFT) of the time domain signals as stated in the following expressions:

$$Z_M(j\omega_k) = \frac{FFT(V_s(t_k))}{FFT(I_s(t_k))}, \quad W_M(j\omega_k) = \frac{FFT(V_h(t_k))}{FFT(V_s(t_k))} \quad (3.2.8)$$

where:  $\omega_k = 2\pi k/NT$ ,  $N$  number of samples per trace,  $T$  sampling period,  $t_k$  sampled time. With the assumption of working in the linear range of the measurement chain, the output voltage  $V_h$  is proportional to the axial pressure field and consequently by (3.2.8)  $W_M(j\omega_k)$  represents the transducer electroacoustic response. In this way, an electroacoustic transfer function have been defined similar to that used by the reciprocity method for the absolute calibration of transducers.

## **CHAPTER 4**

# **DEVELOPMENT OF MATLAB/SIMULINK PULSE-ECHO ULTRASOUND SYSTEM SIMULATOR**

### **4.1 MODELING STRATEGY FOR PULSE-ECHO ULTRASOUND SYSTEM**

Fig. 4.1.1 shows the block diagram of a pulse-echo ultrasound system, consisting of a high-voltage transmitter, a transducer, an ultrasound field, a coaxial cable, and a front-end receiver. In transmit mode, an electrical pulse is generated by the high-voltage transmitter, causing the transducer to produce an acoustic pulse which propagates towards a focal point, reflecting off any object in its path. In receive mode, the transducer picks up the returning acoustic echo, which is converted into an electrical echo signal and processed by the front-end receiver.

The front-end receiver contains a transmit/receive (T/R) switch, which blocks the

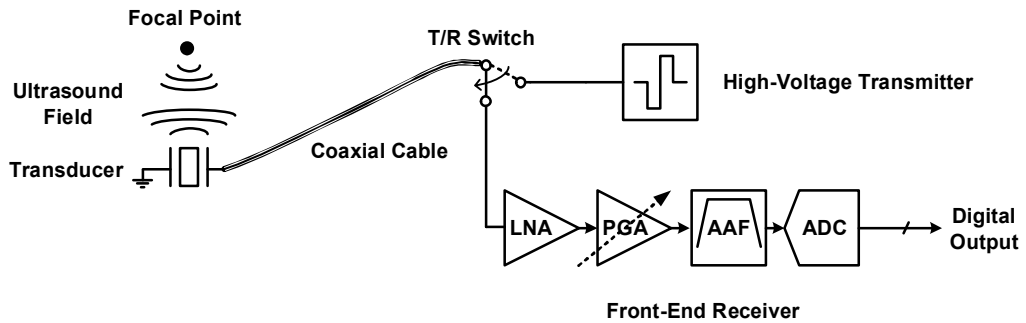


Fig. 4.1.1 Block diagram of a pulse-echo ultrasound system

high-voltage pulses during the reception; a low-noise amplifier (LNA), which acts as a preamplifier; a programmable-gain amplifier (PGA), which provides time-gain compensation to allow for the way in which the returning echo signal is attenuated by body tissues as a function of the distance traveled; an antialiasing filter (AAF), which restricts the bandwidth of the signal to satisfy the Nyquist-Shannon sampling theorem over the band of interest; and an analog-to-digital converter (ADC), which digitizes the electrical echo signal for subsequent image processing [4.1.1].

The block diagram in Fig. 4.1.2 shows the main units of the proposed simulator. A system designer can configure the parameters of the high-voltage transmitter model to generate desired particular high-voltage pulse in transmit mode. The front-end receiver model simulates electrical signal conditioning and analog-to-digital conversion in receive mode, taking into account the most significant non-idealities, such as sampling clock jitter, noise, and harmonic distortion.

The acoustic subsystem that we model consists of a coaxial cable, a transducer and

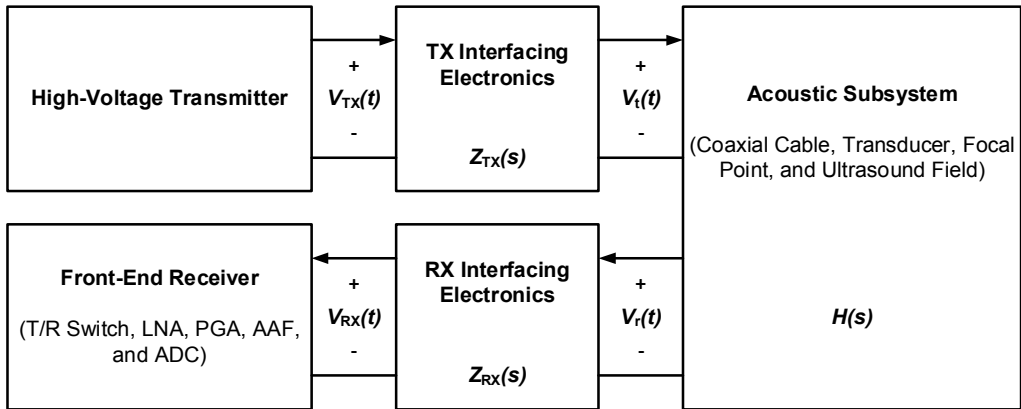


Fig. 4.1.2 Model of the pulse-echo ultrasound system shown in Fig. 1, consisting of five subsystem models. The electronic components in the system are simulated in the high-voltage transmitter model and the front-end receiver model. The acoustic behavior of the ultrasound field and the effect of coaxial cable are modeled as the acoustic subsystem, based on the electroacoustic transfer function  $H(S)$ . To express division of the voltage by the impedances of the subsystems, the transfer functions  $Z_{TX}(S)$  and  $Z_{RX}(S)$ , representing the interfacing electronics, are inserted between the models of the electronics and the acoustic subsystem.

an ultrasound field. The acoustic subsystem model is based on the electroacoustic transfer function  $H(s)$ , which represents the acoustic process which transforms an outgoing electrical pulse  $V_i(t)$  into an incoming electrical echo signal  $V_r(t)$ . This process involves electro-acoustic conversion of the transmitted pulse, acoustic propagation, reflection, and acoustic-electrical conversion of the echo signal.  $H(s)$  can be expressed as the ratio between  $V_i(s)$  and  $V_r(s)$ , which are respectively the Laplace transforms of  $V_i(t)$  and  $V_r(t)$ .

To simulate the voltage division by the impedances of the subsystems, models of the interfacing electronics are inserted between the models of two subsystems. In transmit mode, a model of the TX interfacing electronics acting as a voltage divider based on transfer function  $Z_{TX}(s)$  is inserted between the high-voltage transmitter model and the

acoustic subsystem model. The impedance  $Z_a$  of the acoustic subsystem is the load impedance, as seen by the high-voltage transmitter; and the output impedance  $Z_t$  of the high-voltage transmitter is the source impedance. Thus the amplitude of an electrical pulse  $V_{TX}(t)$  from the high-voltage transmitter needs to be multiplied by  $Z_a/(Z_t+Z_a)$ , if it is to correspond to the electrical pulse  $V_i(t)$  that reaches the acoustic subsystem.

In receive mode, a model of the RX interfacing electronics based on the transfer function  $Z_{RX}(s)$  is inserted between the acoustic subsystem model and the front-end receiver model. The impedance  $Z_a$  of the acoustic subsystem is the source impedance and the input impedance  $Z_r$  of the front-end receiver is the load impedance as seen by the acoustic subsystem connected to the front-end receiver. Thus the amplitude of the electrical echo signal  $V_i(t)$  acquired by the transducer needs to be multiplied by  $Z_r/(Z_a+Z_r)$ , if it is to correspond to the electrical echo signal  $V_{RX}(t)$  that is sent to the front-end receiver.

## 4.2 HIGH-VOLTAGE TRANSMITTER MODEL

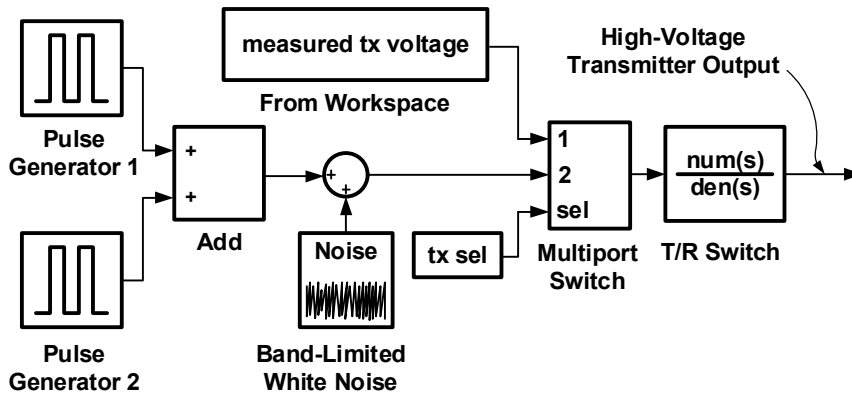


Fig. 4.2.1 Simulink model of the high-voltage transmitter.

Most ultrasound transmitters can be classified as pulse-type or burst-type. Theoretically, an ideal pulse-type transmitter generates a single spike, which is the waveform that produces the best axial resolution. However, a real transducer has a band-pass response, and the pulse that is actually generated needs to be appropriate for the response of that particular transducer. A burst-type transmitter generates several cycles of a square wave or a sinusoid, modulated by a window (such as a Hamming window). Since the amount of energy that can be transmitted into a patient's body is limited by medical authorities, the voltage generated by the transmitter needs to be lower when the pulse train is longer.

Fig. 4.2.1 shows our model, in which the high-voltage transmitter is simulated by relatively simple blocks; nevertheless, the amplitude of the pulse, offset, period and duty

cycles are controllable, and multiple square or sine waves can easily be generated. The best pulse for a particular application can be determined by examining the simulated returning echo signal for different transmitted pulse. Additionally, the multiport switch block allows the simulated output of the high-voltage transmitter to be replaced by measured data.



### 4.3 ACOUSTIC SUBSYSTEM AND INTERFACING ELECTRONICS MODELS

From the description in Section II, the complete transfer function from the transmitted pulse  $V_{TX}(t)$  to the received echo signal  $V_{RX}(t)$  can be written as follows:

$$\frac{V_{RX}(s)}{V_{TX}(s)} = Z_{TX}(s)H(s)Z_{RX}(s) = \frac{Z_a}{Z_t + Z_a}(s)H(s)\frac{Z_r}{Z_a + Z_r}(s), \quad (4.3.1)$$

where  $V_{TX}(s)$  and  $V_{RX}(s)$  are respectively the Laplace transforms of  $V_{TX}(t)$  and  $V_{RX}(t)$ . In order to model this transfer function using Matlab/Simulink, we have measured the output impedance  $Z_t(j2\pi f_k)$  of the high-voltage transmitter and the input impedance  $Z_r(j2\pi f_k)$  of the front-end receiver at 949 frequencies ranging from 1 to 20MHz. To obtain the measured data, Agilent HP4194A impedance analyzer and ECUBE7 ultrasound system are connected by calibrated impedance probe. We have also measured the impedance  $Z_a(j2\pi f_k)$  of the transducer with the 2.3m coaxial cable. The L3-12 transducer that has 128-elements and 8.5MHz center frequency is used in this measurement. Both ECUBE7 ultrasound system and L3-12 transducer are the commercial product developed from Alpinion Medical Systems. Values of the vectors  $Z_a(j2\pi f_k)/(Z_t(j2\pi f_k) + Z_a(j2\pi f_k))$  and  $Z_r(j2\pi f_k)/(Z_a(j2\pi f_k) + Z_r(j2\pi f_k))$  in the complex plane were obtained from the measured data. The transfer functions  $Z_{TX}(s)$  and  $Z_{RX}(s)$  were then computed using the *rationalfit* function in Matlab to fit a function of the following form

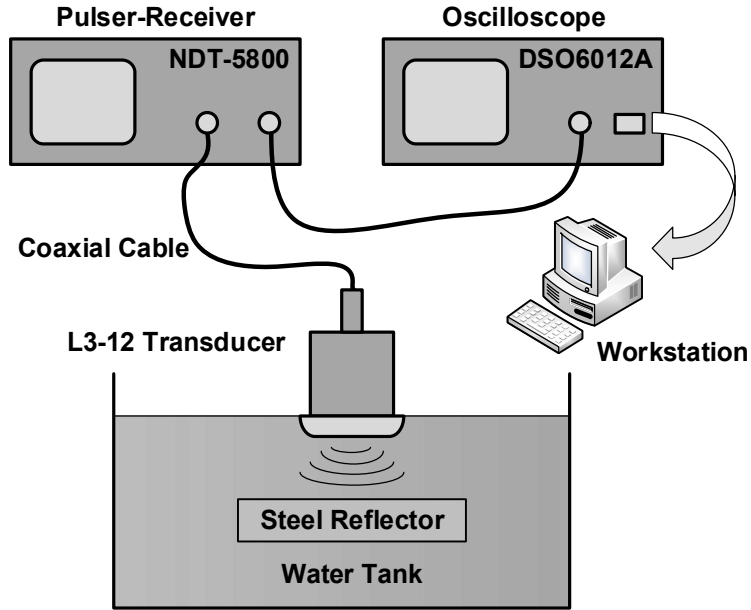


Fig. 4.3.1 Setup for the pulse-echo measurements required to build the electroacoustic transfer function  $H(s)$ .

to the complex vector data [4.3.1], [4.3.2]:

$$F(s) = \sum_{k=1}^N \frac{\text{residue}_k}{s - \text{pole}_k}, \quad (4.3.2)$$

where  $N$  is the number of poles.

We also need to measure  $V_t(j2\pi f_k)$  and  $V_r(j2\pi f_k)$  in the frequency domain, in order to build the transfer function  $H(s)$ . We made pulse-echo measurements using the setup shown in Fig. 4.3.1. A Panametrics NDT-5800 pulser-receiver sends a high-voltage pulse to the transducer, which sends an acoustic wave towards a steel reflector in a water tank,

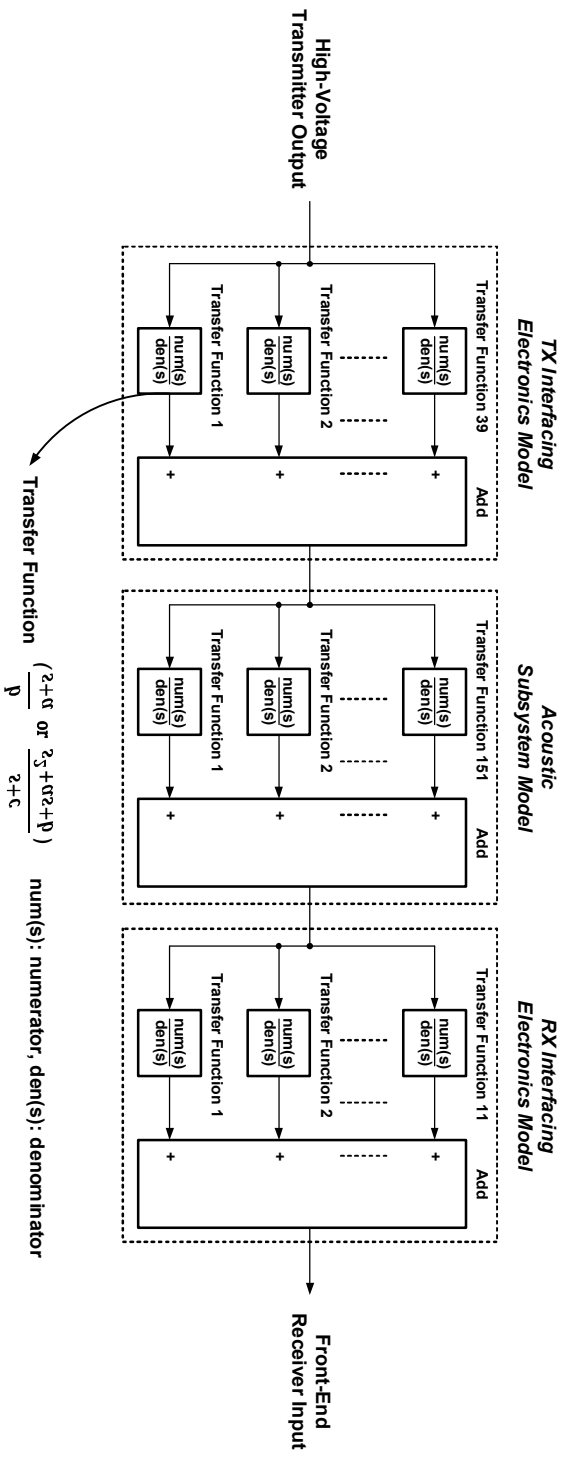


Fig. 4.3.2 Simulink models of the TX interfacing electronics, acoustic subsystem, and RX interfacing electronics, based respectively on the transfer functions  $Z_{\text{TX}}(s)$ ,  $H(s)$ , and  $Z_{\text{RX}}(s)$ .

and awaits echoes. The echoes received by the pulser-receiver are measured using an Agilent DSO6012A oscilloscope, which samples the echo signal every 5ns, and transfers the digitized sample to a workstation. Measurements of  $V_t(t_k)$  and  $V_r(t_k)$  at sampling time  $t_k$  are converted respectively into  $V_t(j2\pi f_k)$  and  $V_r(j2\pi f_k)$ , in the frequency domain, by discrete Fourier transform.  $V_t(j2\pi f_k)$  is the product of  $V_{TX}(j2\pi f_k)$  and  $Z_a(j2\pi f_k)/(Z_t(j2\pi f_k)+Z_a(j2\pi f_k))$ . From this frequency domain data, we can find  $H(j2\pi f_k)$  from the ratio  $V_r(j2\pi f_k)/V_t(j2\pi f_k)$ . We can then compute  $H(s)$  by calling the *rationalfit* function, as we did to obtain  $Z_{TX}(s)$  and  $Z_{RX}(s)$ . The transducer has its own axial intensity profile, so the magnitude of the transfer function  $H(s)$  changes depending on the distance between the transducer and the reflector. However, the transducer's significant properties in the system-level optimization, such as center frequency, bandwidth, and impedance, are not affected by the distance. Therefore, the overall direction of system development does not change. In our experiment, we have measured transducer properties with 20mm distance that is focal depth of the transducer. Although the distance between transducer and steel reflector can slightly affect transfer function  $H(s)$  with the attenuation of medium, we assume that the attenuation coefficient of water (0.0022dB/MHz/cm) is small enough to be neglected for our study.

The Simulink models of the TX interfacing electronics, the acoustic subsystem, and the RX interfacing electronics consist of a number of transfer function blocks, together with an add block. The poles and relevant residues of a transfer function can be converted respectively to the numerator and denominator of a transfer function block in the Simulink environment, as shown in Fig. 4.3.2.  $Z_{TX}(s)$ ,  $H(s)$  and  $Z_{RX}(s)$  has 77, 300, and 19

poles respectively. To ensure that every transfer function block has real coefficients, each block represents either one real pole, or a pair of complex conjugate poles. Consequently, each Simulink model of the TX interfacing electronics, acoustic subsystem, and RX interfacing electronics has 39, 151, and 11 transfer function blocks.

## 4.4 FRONT-END RECEIVER MODEL

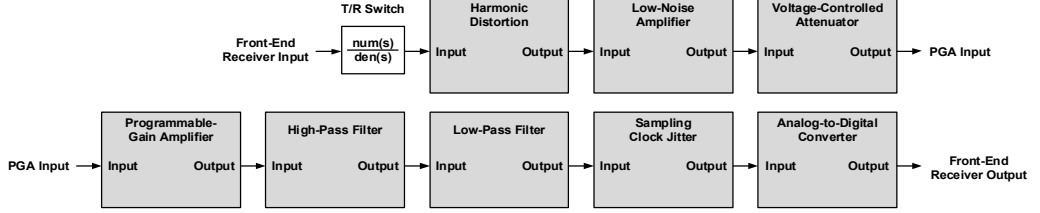


Fig. 4.4.1 Simulink model of the front-end receiver.

Our Simulink model of a front-end receiver, shown in Fig. 4.4.1, consists of a transfer function block, the T/R switch, and eight subsystem blocks, which model: harmonic distortion, the low-noise amplifier (LNA), the voltage-controlled attenuator (VCAT), the programmable-gain amplifier (PGA), the high-pass filter (HPF), the low-pass filter (LPF), sampling clock jitter, and the analog-to-digital converter (ADC).

### 4.4.1 T/R SWITCH AND ACTIVE TERMINATION

Fig. 4.4.2 shows an equivalent circuit model of the T/R switch [4.4.1]. The values of  $R_s$ ,  $R_p$  and  $C_p$  are  $13\Omega$ ,  $100k\Omega$  and  $40pF$  respectively.  $R_{IN}$  and  $C_{IN}$  are the input resistance and the input capacitance of the LNA.  $R_F$  is a shunt feedback resistor for an active input termination, which is preferred in ultrasound applications because it reduces the reflections resulting from mismatches and achieves better axial resolution without a

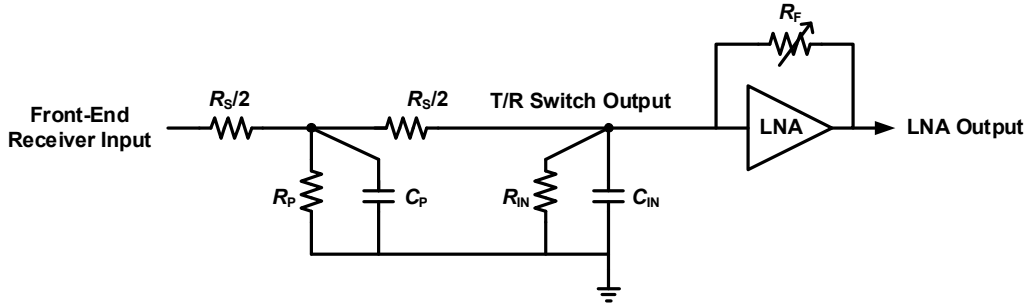


Fig. 4.4.2 Equivalent circuit model of the T/R switch under considering the active input termination.

significant increase in noise. The input impedance  $Z_{IN, \text{Active Termination}}$  of the LNA under the active termination approximately follows:

$$Z_{IN, \text{Active Termination}} = \frac{R_F}{1 + \frac{A_{V, \text{LNA}}}{2}}, \quad (4.4.1)$$

where,  $A_{V, \text{LNA}}$  is the voltage gain of the LNA. The equivalent input impedance of the LNA can be expressed as follows [4.4.2]:

$$Z_{IN}(s) = Z_{IN, \text{Active Termination}} \parallel R_{IN} \parallel C_{IN} = \frac{R_{IN} R_F}{R_F R_{IN} C_{IN} s + \left(1 + \frac{A_{V, \text{LNA}}}{2}\right) R_{IN} + R_F}. \quad (4.4.2)$$

Without active termination, the value of the feedback resistor  $R_F$  is effectively infinite. The transfer function of the T/R switch under the active termination configuration can be expressed as follows:

$$\frac{V_{\text{T/R Switch Output}}}{V_{\text{Front-End Receiver Input}}}(s) = \frac{2R_p}{R_s R_p C_p s + R_s + 2R_p} \cdot \frac{2Z_{\text{IN}}(s)}{R_s + 2Z_{\text{IN}}(s)} . \quad (4.4.3)$$

The transfer function block which models the T/R switch is shown at the top left in Fig. 4.4.1.



#### 4.4.2 HARMONIC DISTORTION

Fig. 4.4.3 shows the model of harmonic distortion. The model is placed between T/R switch and the LNA to express the signal distortion introduced by the nonlinearities of the amplifiers and ADC in the front-end receiver. The harmonic distortion is not shown in Fig. 4.4.2, because it is not a specific circuit but a phenomenon from following circuits.

The parameter value of the constant block controls the order of the harmonic distortion, and the gain changes its power. By describing a transfer function in polynomial form:

$$y = \alpha_0 + \alpha_1 x + \alpha_2 x^2 + \alpha_3 x^3 \dots \quad (4.4.4)$$

Next, variable  $x$  is replaced by a single tone input given by  $A \cos(\omega t)$ . Hence, after some algebraic manipulations:

$$y = \left( \alpha_1 A - \frac{\alpha_3 A^3}{4} \right) \cos \omega t - \frac{\alpha_3 A^3}{4} \cos 3\omega t \quad (4.4.5)$$

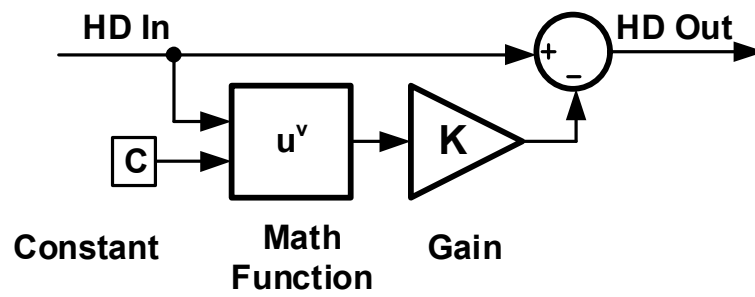


Fig. 4.4.3 Simulink model of harmonic distortion.

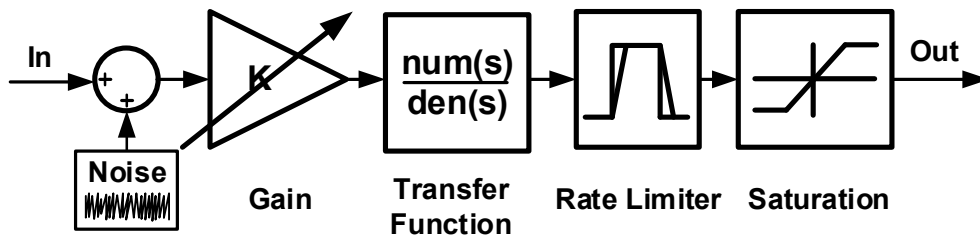


Fig. 4.4.4 Simulink model of LNA, VCAT and VGA with variable gain.

### 4.4.3 AMPLIFIER AND FILTER

Fig. 4.4.4 shows the model of the amplifier used in the LNA, VCAT and PGA subsystem blocks. The gain and transfer function model the amplifier's finite gain and bandwidth. The rate limiter models the amplifier's slew-rate, and the saturation block models the output swing. Our Simulink model of the front-end receiver also includes a model of amplifier noise, which is a crucial difference between a real and an ideal circuit. This amplifier noise is made up of current and voltage noise, together with thermal noise from the source resistance. Several noise-modeling blocks have been introduced into the LNA, VCAT and PGA subsystem blocks to simulate the band-limited white noise of the input voltage, current noise from the LNA, and the input voltage noise from the PGA and VCAT. The total voltage-noise density of the output of the amplifier can be expressed as follows:

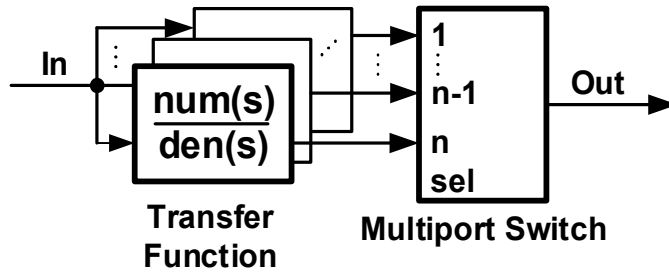


Fig. 4.4.5 Simulink model of HPF and LPF with selective bandwidth.

$$E_O = \sqrt{e_N^2 + (i_N R_{\text{source}})^2 + 4K_B T R_{\text{source}}} , \quad (4.4.6)$$

where  $e_N$  is the voltage noise density of the amplifier. The term  $i_N R_{\text{source}}$  is the product of the voltage contribution of current-noise density and the source resistance, which has a thermal-noise density of  $(4K_B T R_{\text{source}})^{1/2}$ . The source resistance  $R_{\text{source}}$  is the impedance of the transducer, and is therefore likely to vary widely with the type of transducer in use. Fig. 4.4.5 shows the HPF and LPF subsystems, in each of which the filter is represented by a transfer function, and this can be changed using the multiport switch to vary the bandwidth of the corresponding filter.

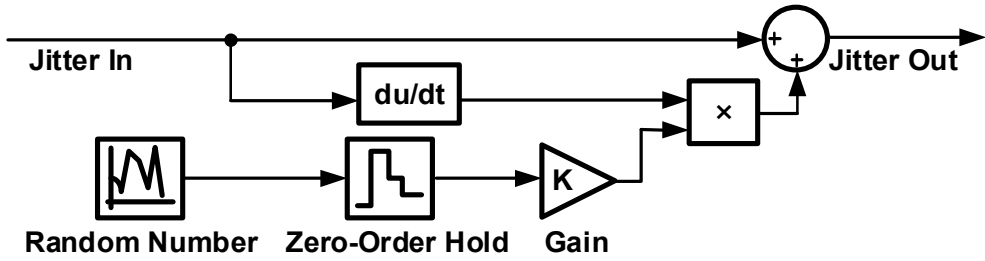


Fig. 4.4.6 Simulink model of sampling clock jitter.

#### 4.4.4 SAMPLING CLOCK JITTER

Fig. 4.4.6 shows the model of sampling clock jitter, defined as a random variation of the sampling instant; the resulting noise is assumed to be uniformly distributed. Clock jitter results in a non-uniform sampling time sequence, and produces an error which increases the total error power at the spectrum output of the ADC. The error introduced in Fig. 4.4.7 by a sinusoidal signal  $x(t)$  with amplitude  $A$  and frequency  $f_{\text{in}}$  can be calculated as in terms of the jitter deviation  $\delta$  as follows [4.4.3]:

$$x(t + \delta) - x(t) \approx 2\pi f_{\text{in}} \delta A \cos(2\pi f_{\text{in}} t) = \delta \frac{dx(t)}{dt}, \quad (4.4.7)$$

and (4.4.7) is the basis of our jitter model.

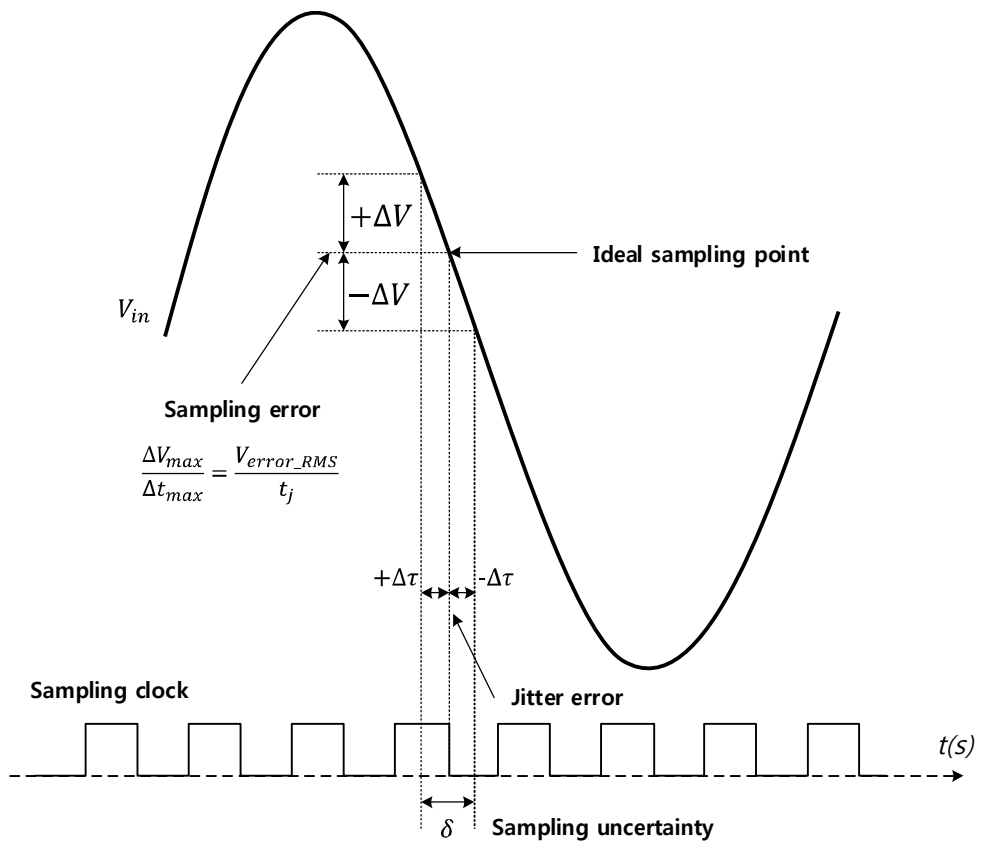


Fig. 4.4.7 Sampling clock jitter.

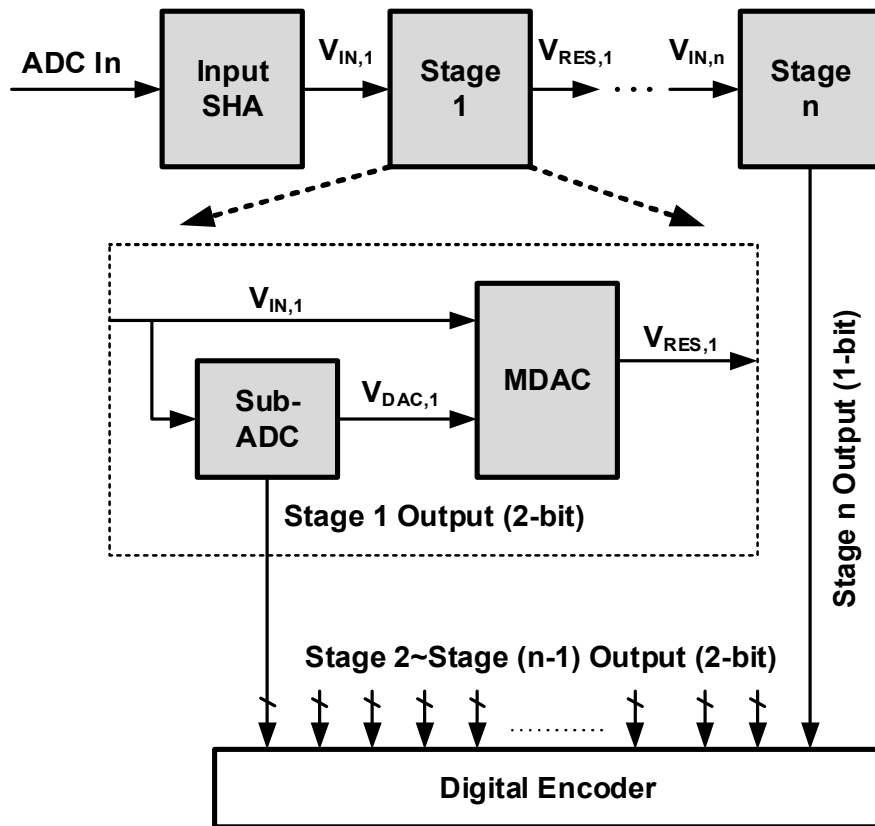


Fig. 4.4.8 Simulink model of ADC.

#### 4.4.5 ANALOG-TO-DIGITAL CONVERTER

The ADC in an ultrasound system requires a sampling-rate which is at least 40MS/s, and a resolution between 10 and 14bits. A pipelined ADC architecture is known to be able to satisfy these requirements, and that is what we have modeled as shown in Fig. 4.4.8.

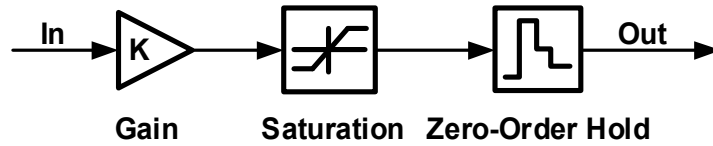


Fig. 4.4.9 Simulink model of input SHA in ADC.

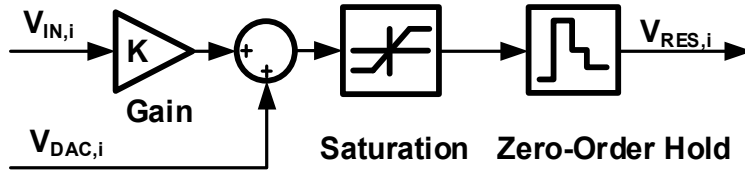


Fig. 4.4.10 Simulink model of MDAC in  $i$ th stage.

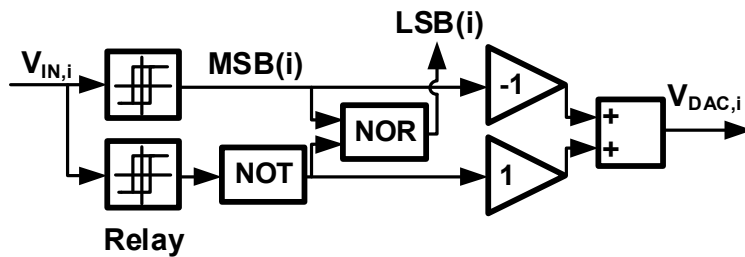


Fig. 4.4.11 Simulink model of sub-ADC in  $i$ th stage.

This ADC includes a sample-and-hold amplifier (SHA), several stages, and an encoder for digital correction, and each stage has a multiplying DAC (MDAC) and a sub-ADC. Fig. 4.4.9, Fig. 4.4.10 and Fig. 4.4.11 respectively show the block diagrams of the SHA, the MDAC, and the sub-ADC which is inside the ADC. The digital encoder is described using a Matlab script.



# CHAPTER 5

## EXPERIMENTS VERSUS SIMULATION

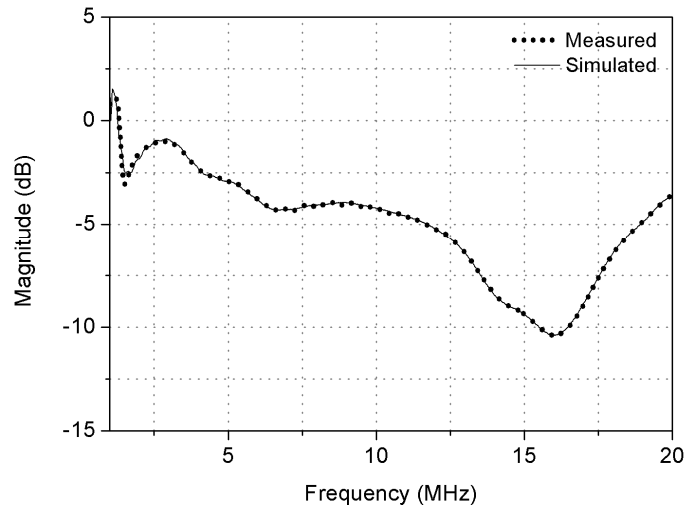
### 5.1 VALIDATION OF SUBSYSTEMS

#### 5.1.1 ACOUSTIC SUBSYSTEM AND INTERFACING ELECTRONICS

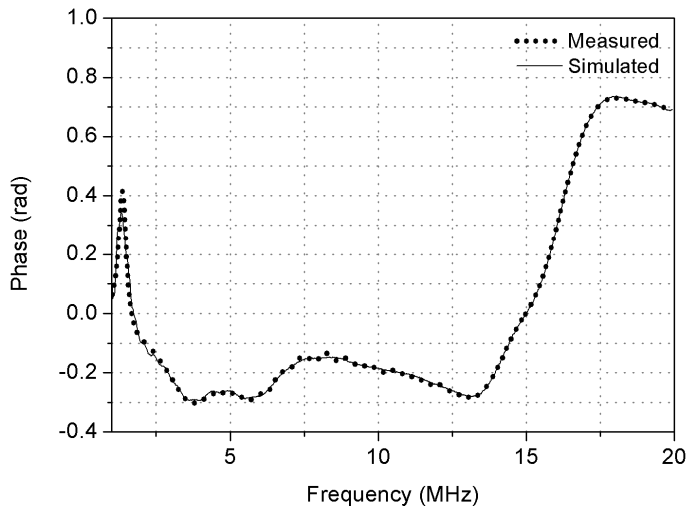
Before simulating the complete ultrasound system, we assessed the accuracy of each subsystem model. We started with the models of the acoustic subsystem and the interfacing electronics, and investigated the accuracy of the approximate transfer functions  $Z_{TX}(s)$ ,  $H(s)$ , and  $Z_{RX}(s)$  in the same context as shown in [5.1.1]. Fig. 5.1.1 compares the approximate transfer function  $Z_{TX}(s)$  obtained by calling the *rationalfit* function with the complex vector data  $Z_a(j2\pi f_k)/(Z_t(j2\pi f_k)+Z_a(j2\pi f_k))$ , measured using an Agilent HP4194A impedance analyzer at 949 frequencies in the frequency domain. The difference between the curves can be expressed as follows:

$$10^{\varepsilon/20} \geq \frac{\sqrt{\sum_{k=1}^n |F_0\{f_k\} - F(s)|^2}}{\sqrt{\sum_{k=1}^n |F_0\{f_k\}|^2}}, \quad (5.1.1)$$

where  $\varepsilon$  is the error in dB,  $F_0$  is the measured value of  $F_0(j2\pi f_k)$  at a frequency  $f_k$ ,  $F(s=j2\pi f)$  is the approximation of the transfer function computed using the *rationalfit* function. On this basis, the error in  $Z_{TX}(s)$  is -32.18dB. Fig. 5.1.2 shows similar results for  $H(s)$ , and here the error is -43.83dB. At around 17.5MHz there is a mismatch between the simulated and the measured signals, but this frequency is sufficiently distant from the carrier frequency that it contains no meaningful information. Fig. 5.1.3 shows further results for the transfer function  $Z_{RX}(s)$ , and in this case the error is less than -44dB.

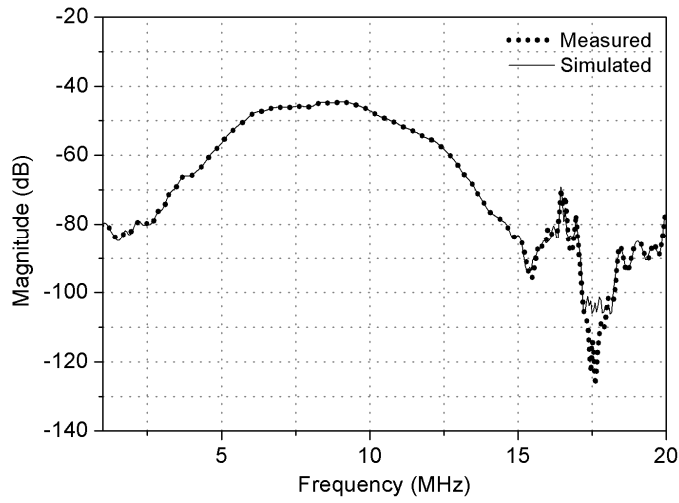


(a)

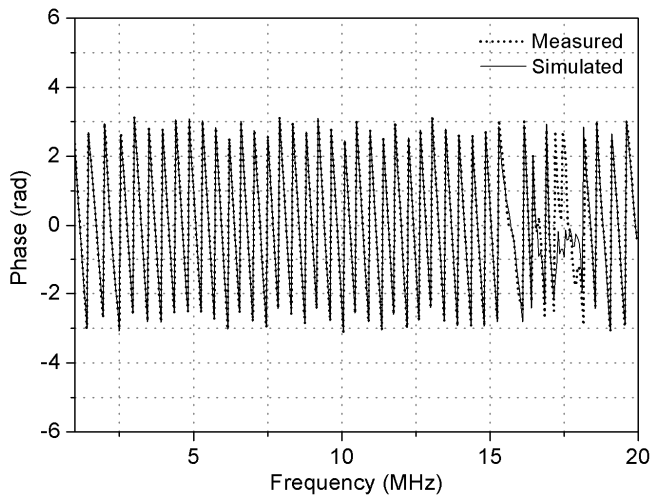


(b)

Fig. 5.1.1 Comparison between the transfer function  $Z_{TX}(s)$  and the experimental data  $Z_{TX}(j2\pi f_k)$  (a) magnitude and (b) phase, both against the frequency  $f_k$ .

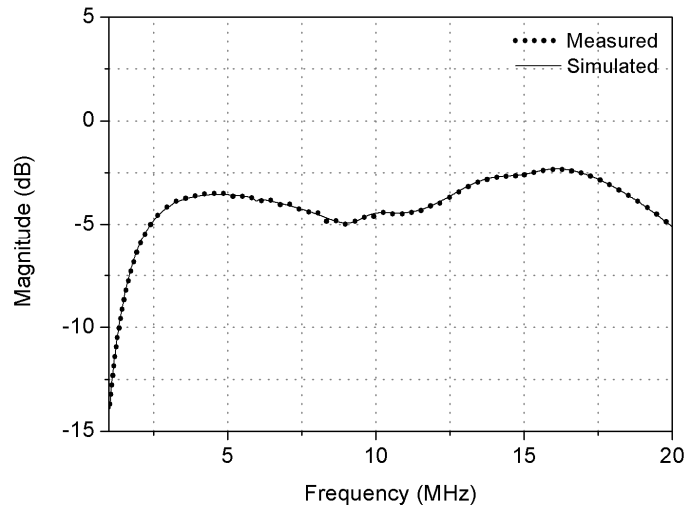


(a)

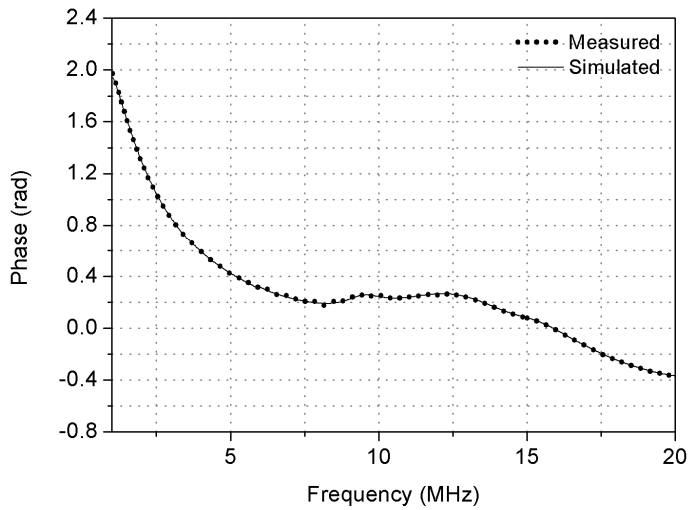


(b)

Fig. 5.1.2 Comparison between the transfer function  $H(s)$  and the experimental data  $H(j2\pi f_k)$  (a) magnitude and (b) phase, both against the frequency  $f_k$ .



(a)



(b)

Fig. 5.1.3 Comparison between the transfer function  $Z_{RX}(s)$  and the experimental data  $Z_{RX}(j2\pi f_k)$  (a) magnitude and (b) phase, both against the frequency  $f_k$ .

### 5.1.2 FRONT-END RECEIVER

We then turned to the model of the front-end receiver. We sent a sine wave with an amplitude of  $8\text{mV}_{\text{pp}}$  and frequency of  $5\text{MHz}$  to both the Matlab/Simulink model and the front-end receiver in the ECUBE7 ultrasound system. The parameters of the front-end receiver, obtained from its datasheet [5.1.3], are summarized in Table I. The ability of our entire simulation, to predict system performance and image quality, depends on accurate modeling of the noise characteristics of the front-end receiver [5.1.4]. We can see from (4.4.6) that the controllable parameters related to the noise of the front-end receiver include the source impedance, and the gain of the LNA and PGA. The source impedance contributes to the second and third terms in (4.4.6), which are the densities of input current noise and thermal noise. The gain of the LNA and PGA affect the first term of (4.4.6) which is the input voltage noise density [5.1.4]. We compared the narrow-band signal-to-noise ratio (NBSNR) of the simulated and measured results for different combinations of LNA and PGA gain, and different source impedances. The source impedance of the front-end receiver was changed by inserting termination resistors with values of  $50$ ,  $120$  and  $240\Omega$  between the input of the front-end receiver and ground. We also compared the spurious-free dynamic range (SFDR) of the simulated and measured results to assess the accuracy with which distortion is modeled. Tables II and III compare measured values of NBSNR and SFDR with simulation results.

Table 2.1.1 Front-end receiver parameters in the Matlab/Simulink model

Parameter	Value	Units
Low-Noise Amplifier (LNA)		
Input resistance	8	k $\Omega$
Input capacitance	20	pF
Gain	12, 18, 24	dB
Bandwidth	70	MHz
Input voltage noise over gain	0.9, 0.7, 0.63	nV/ $\sqrt{\text{Hz}}$
Input current noise	2.7	pA/ $\sqrt{\text{Hz}}$
Voltage Controlled Attenuator (VCAT)		
Attenuation	0 to -40 (9 steps)	dB
Input voltage noise over attenuation	2 to 10.5 (9 steps)	nV/ $\sqrt{\text{Hz}}$
Programmable Gain Amplifier (PGA)		
Gain	24, 30	dB
Bandwidth	70	MHz
Input voltage noise	1.75	nV/ $\sqrt{\text{Hz}}$
Full-scale range	3.3	V
Anti-Aliasing Filter (AAF)		
Low cut-off frequency	50, 100, 150	kHz
High cut-off frequency	10, 15, 20, 30	MHz
Analog-to-Digital Converter		
Sampling clock jitter	20	ps
Input range	2	V
Sampling-rate	40, 65	MS/S
Resolution	12, 14	bits

Table 2.1.2 Measured and simulated values of NBSNR of the front-end receiver for different combinations of LNA and PGA gain, and with different termination resistors

Termination Resistor ( $\Omega$ )	LNA Gain (dB)	PGA Gain (dB)	Measured NBSNR* (dB)	Simulated NBSNR* (dB)	Error (dB)
50	12	24	39.68	39.42	0.26
		30	38.68	39.42	-0.74
	18	24	40.48	40.82	-0.34
		30	40.41	40.86	-0.45
	24	24	40.99	41.5	-0.51
		30	42.05	41.52	0.53
120	12	24	45.82	44.66	1.16
		30	44.61	45.06	-0.45
	18	24	45.52	46.07	-0.55
		30	45.55	46.08	-0.53
	24	24	45.83	46.65	-0.82
		30	50.14	46.68	3.46
240	12	24	48.68	48.16	0.52
		30	48.06	48.26	-0.2
	18	24	50	49.1	0.9
		30	49.07	49.15	-0.08
	24	24	48.18	49.52	-1.34
		30	50.14	49.58	0.56

\*NBSNR (dB) =  $10 \times \log_{10}(\text{signal power}(V_{\text{rms}}^2) / \text{sum of noise power in 2MHz band around signal frequency}(V_{\text{rms}}^2))$



Table 2.1.2 Measured and simulated values of SFDR of the front-end receiver for different combinations of LNA and PGA gain, and with different termination resistors

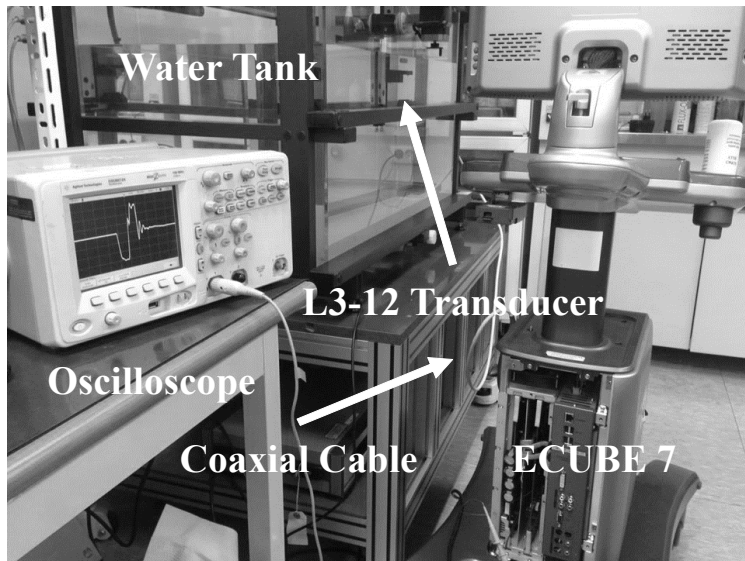
Termination Resistor ( $\Omega$ )	LNA Gain (dB)	PGA Gain (dB)	Measured SFDR (dB)	Simulated SFDR (dB)	Error (dB)
50	12	24	41.54	48.52	-6.98
		30	43.7	48.03	-4.33
	18	24	43.51	49.79	-6.28
		30	45.25	49.77	-4.52
	24	24	49.08	50.87	-1.79
		30	49.74	50.55	-0.81
120	12	24	51.3	54	-2.7
		30	54.95	54.52	0.43
	18	24	51.48	55.5	-4.02
		30	52.05	55.11	-3.06
	24	24	51.28	55.85	-4.57
		30	55.32	55.65	-0.33
240	12	24	55.94	54.42	1.52
		30	55.51	54.66	0.85
	18	24	55.82	54.1	1.72
		30	58.05	54.34	3.71
	24	24	50.11	54.21	-4.1
		30	55.97	54.3	1.67

We assessed our model of the high-voltage transmitter as part of our validation of the complete system by comparing the simulated output waveform of the model to measured high-voltage pulses while inputting the same parameters to the signal generator block in the model and the high-voltage transmitter in the ECUBE7 ultrasound system.

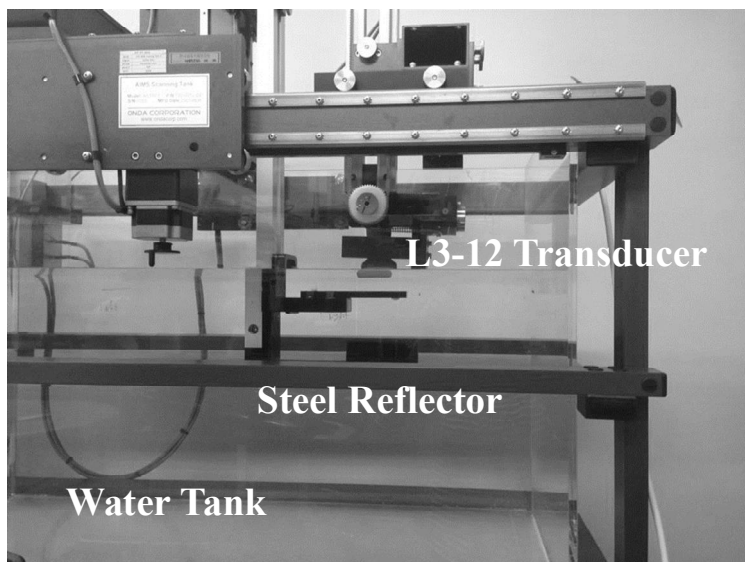
## **5.2      VALIDATION OF COMPLETE SYSTEM**

### **5.2.1   EXPERIMENTAL SETUP**

After they had been checked individually, the sub-system models were integrated in to a system model. We then carried out experiments on the complete system to verify correct pulse-echo operation. The experimental setup is shown in Fig. 5.2.1. The L3-12 transducer immersed in a water tank is connected by a coaxial cable to an ECUBE7 ultrasound system. The transducer is excited by pulses from the high-voltage transmitter in the ECUBE7, and produces the ultrasonic waves which propagate through the water and are reflected by a steel reflector. By exciting the transducer with a low voltage signal (tens of volts), it is possible to avoid the nonlinearity of the water [5.2.1]. The same transducer converts the returning sound to an electrical echo signal. The transmitted high-voltage pulse and received echo signal can be visualized on an oscilloscope. The electrical echo signal goes through amplification, filtering, analog-to-digital conversion by the front-end receiver in the ECUBE7.

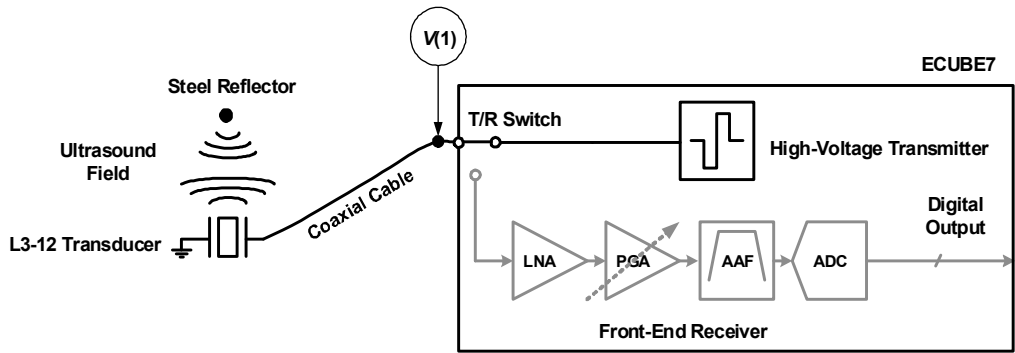


(a)

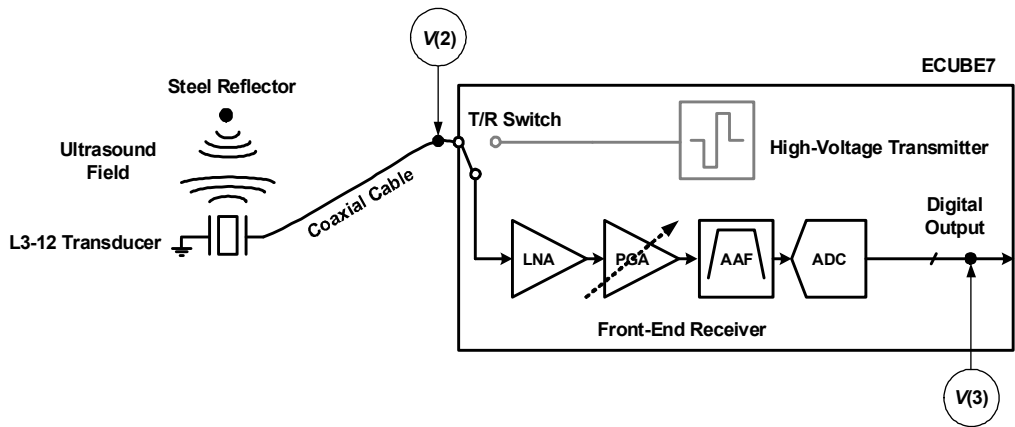


(b)

Fig. 5.2.1. Photographs of (a) our experimental setup with (b) the water tank.



(a)



(b)

Fig. 5.2.2. Block diagram of a pulse-echo ultrasound system in (a) transmit and (b) receive mode.

Fig. 5.2.2 shows block diagrams of the experimental setup with the pulse-echo ultrasound system operating in transmit and receive modes.  $V(1)$  is the electrical pulse from the high-voltage transmitter,  $V(2)$  is the electrical echo signal from the acoustic subsystem, and  $V(3)$  is the digital output of the front-end receiver. The high-voltage pulse

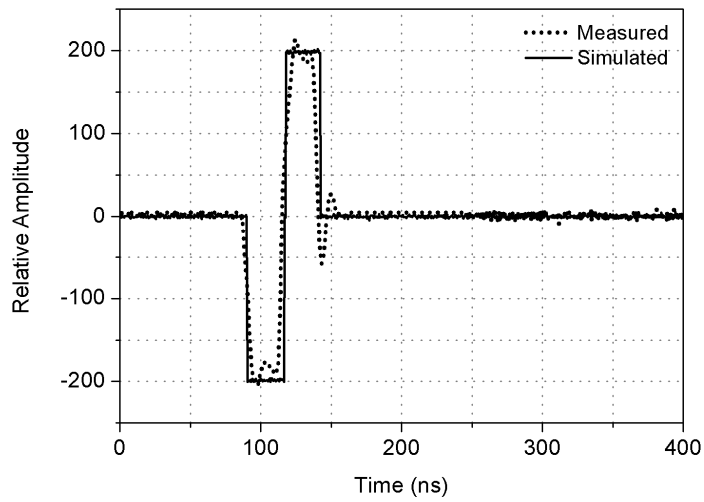
$V(1)$  and the echo signal  $V(2)$  were sampled every 5ns, and the digital output of the echo signal  $V(3)$  was acquired every 25ns. Agilent 10076C high-voltage probe, which supports maximum 4kV input voltage, was used to measure the high-voltage pulse  $V(1)$ .

## 5.2.2 COMPARISON SIMULATION AND MEASUREMENTS

We will now compare the signals obtained from experiments and simulations. Fig. 5.2.3 compares the measured waveform of the high-voltage pulse  $V(1)$  in Fig. 5.2.2 with the simulated waveform from the high-voltage transmitter model. The amplitudes of these signals are normalized, so the received echo signal has a peak amplitude of unity. We are able to input either the measured or the simulated version of this waveform to the acoustic subsystem in our simulation; but we found that this produces no appreciable difference to the received echo signal, suggesting that the waveforms are very similar indeed.

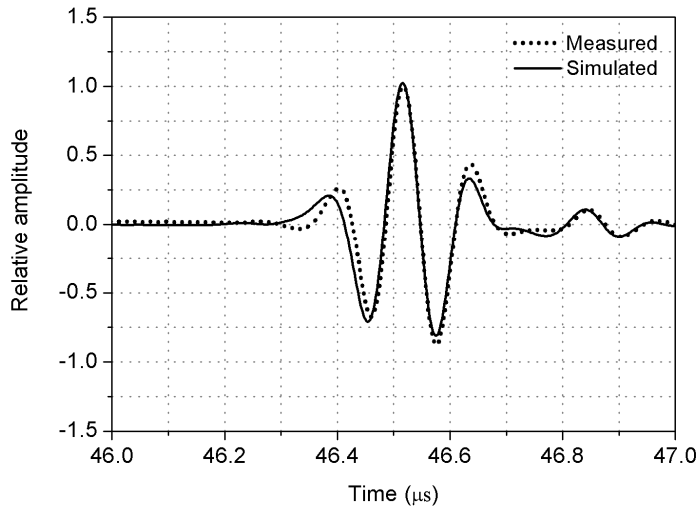
Fig. 5.2.4 compares the waveform of the received echo signal  $V(2)$  in Fig. 5.2.2, measured between the acoustic subsystem and the front-end receiver, with the simulated waveform from the acoustic subsystem model. In Fig. 5.2.5(a), there is a noticeable divergence around  $46.4\mu\text{s}$ ; otherwise, the curves show satisfactory agreement. Fig. 5.2.6 shows the digitized output  $V(3)$  in Fig. 5.2.2 from the front-end receiver at a sampling rate of 40MSPS.

Overall, these results suggest that our system model simulates the system-level behavior of a pulse-echo ultrasound system with sufficient fidelity to give it a place in the design process.

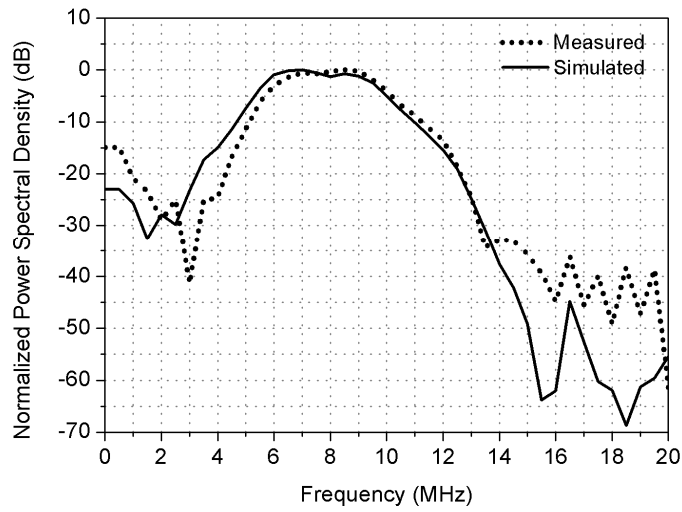


(a)

Fig. 5.2.3. Measured and simulated amplitudes of the high-voltage pulse  $V(1)$ .



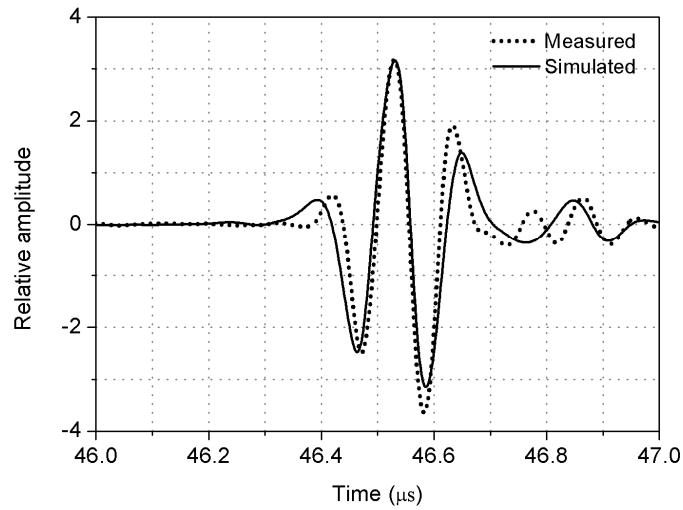
(a)



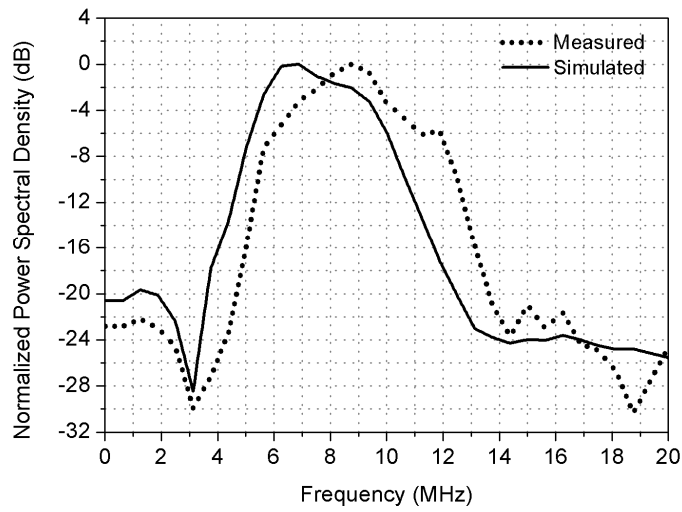
(b)

Fig. 5.2.4. Measured and simulated amplitudes of the echo signal  $V(2)$  (a) in the time domain and (b) in the frequency domain.





(a)



(b)

Fig. 5.2.5. Measured and simulated amplitude of the digitized output  $V(3)$  (a) in the time domain and (b) in the frequency domain.

### 5.3 DISCUSSION

One immediate application of our model is the design of a matching network, which can be implemented as a parallel compensating inductance, a series compensating inductance, or an ‘L’ matching network [5.3.1]. If we use a series compensating inductance, for example, then we need to change the imaginary part of the transducer impedance  $Z_a$ . We can do this by adding a term  $2\pi f_k L$  to the measured transducer impedance  $Z_a$ , recomputing the transfer functions  $Z_{TX}(s)$  and  $Z_{RX}(s)$ , and rebuilding the Simulink model of the interfacing electronics.

We would expect to achieve more accurate matching than existing simulators, which model the ultrasound field but not the electronics. In particular it is unsatisfactory to ignore the impedances of the high-voltage transmitter and the front-end receiver, and thus selected values of the inductors may be far from optimal in the context of the whole system. This means that the matching network has to be redesigned for each transducer, and tested at the imaging level. Our simulator should reduce the need for these activities.

Our simulation can also help in choosing a good shape for the electrical pulse generated by the high-voltage transmitter, because a designer can observe the simulated echo signal as the shape of the transmitted pulse is changed. A designer can also search for system parameters which improve the final SNR, because the simulation includes the analog processes of amplification, filtering and A/D conversion which take place in the front-end receiver. We can determine the most appropriate components in the front-end receiver by considering application requirements: the maximum gain required from the

amplifiers and an acceptable density of input referred noise are both determined by the depth of the target to be imaged; the resolution of the ADC is determined by the required image quality; and also, the bandwidth of the LNA and PGA, the cut-off frequency of the AAF, and the sampling rate of the ADC all depend on the bandwidth of the transducer used in a particular application.

## CHAPTER 6

### CONCLUSIONS

We have presented a simulator for pulse-echo ultrasound systems, which combines models the high-voltage transmitter, coaxial cable, transducer, ultrasound field, and front-end receiver in a single Matlab/Simulink simulation. A system designer can generate the high-voltage pulses that they require by configuring the input parameters of the high-voltage transmitter model. The acoustic subsystem model, which consists of the coaxial cable, transducer, and ultrasound field, is based on samples of the transmitted pulse and received echo. From these samples, a transfer function of the acoustic subsystem is formulated in the Laplace s-domain using the Matlab *rationalfit* function, and is then converted to a Simulink model. To express the voltage division caused by impedances, models of the interfacing electronics one for transmit and one for receive mode, are inserted between subsystems. These models are also based on transfer functions, which are obtained by measuring the impedance of the acoustic subsystem, the high-voltage transmitter, and the front-end receiver. The model of the front-end receiver includes the main non-idealities (i.e. amplifier noise, harmonic distortion, and sampling clock jitter) which have the potential to reduce system performance significantly.

This simulator is intended to facilitate the design of matching networks and system optimization. In particular, the availability of a model of the high-voltage transmitter

makes it easier to discover how characteristics of the transmitted pulse, such as its magnitude and frequency, the number of peaks, rise and fall times, and jitter and noise, will affect the received echo. Designers can also examine the effects of the front-end receiver parameters on the whole system. We have demonstrated that our simulator is accurate enough to contribute to the development of ultrasound systems by comparing the simulated results with measured data from a commercial ultrasound system.

# BIBLIOGRAPHY

- [1.1.1] Thomas L. Szabo, “Diagnostic Ultrasound Imaging: Inside Out,” Elsevier Academic Press, 2004.
- [1.1.2] Charles J. Pavlin and F. Stuart Foster, “Ultrasound Biomicroscopy of the Eye,” Springer-Verlag New York, Inc., 1994.
- [1.3.1] B. A. J. Angelsen, H. Torp, S. Holm, K. Kristoffersen, and T. A. Whittingham, “Which transducer array is best?” *Eur. J. Ultrasound*, vol. 2, no. 2, pp. 151–164, 1995.
- [1.3.2] H. Huang and D. Paramo, “Broadband electrical impedance matching for piezoelectric ultrasound transducers,” *IEEE Trans. Ultrason. Ferroelectr. Freq. Control*, vol. 58, no. 12, pp. 2699–2707, Dec. 2011.
- [1.3.3] E. Brunner, “Ultrasound system considerations and their impact on front-end components,” *Analog Dialogue*, Analog Devices Inc., vol. 36, no. 3, 2002.
- [1.3.4] A. Püttmer, P. Hauptmann, R. Lucklum, O. Krause, and B. Henning, “SPICE model for lossy piezoceramic transducers,” *IEEE Trans. Ultrason., Ferroelect., Freq. Control*, vol. 44, no. 1, pp. 60–66, Jan. 1997.
- [1.3.5] E. Maione, P. Tortoli, G. Lypacewicz, A. Nowicki, and J. M. Reid, “PSpice modelling of ultrasound transducers: comparison of software models to experiment,” *IEEE Trans. Ultrason., Ferroelect., Freq. Control*, vol. 46, no. 2, pp. 399–406, Mar. 1999.
- [1.3.6] J. van Deventer, T. Lofqvist, and J. Delsing, “PSpice simulation of ultrasonic systems,” *IEEE Trans. Ultrason., Ferroelect., Freq. Control*, vol. 47, no. 4, pp. 1014–1024, Jul. 2000.
- [1.3.7] R. Guelaz, D. Kourtiche, and M. Nadi, “Ultrasonic piezoceramic transducer modeling with VHDL-AMS: application to ultrasound nonlinear parameter simulations,” *IEEE Sensors J.*, vol. 6, no. 6, pp. 1652–1661, Dec. 2006.
- [1.3.8] J. Johansson, P.-E. Martinsson, and J. Delsing, “Simulation of absolute

- amplitudes of ultrasound signals using equivalent circuits,” IEEE Trans. Ultrason. Ferroelectr. Freq. Control, vol. 54, no. 10, pp. 1977–1982, Oct. 2007.
- [1.3.9] N. Aouzale, A. Chitnalah, and H. Jakjoud. "Experimental validation of SPICE modeling diffraction effects in a pulse-echo ultrasonic system," IEEE Trans. Circuits Syst. II, Exp. Briefs, vol. 56, no. 12, pp. 911–915, Dec. 2009.
- [1.3.10] W. P. Mason, *Electromechanical Transducers and Wave Filters*, Van Nostrand, 1948.
- [1.3.11] M. Redwood, “Transient performance of a piezoelectric transducer,” J. Acoust. Soc. Am., vol. 33, no. 4, pp. 527–536, Apr. 1961.
- [1.3.12] R. Krimholtz, D. A. Leedom, and G. L. Matthaei, “New equivalent circuit for elementary piezoelectric transducers,” Electron. Lett., vol. 6, no. 13, pp. 398–399, Jun. 1970.
- [1.3.13] W. Marshall Leach, Jr., “Controlled-source analogous circuits and SPICE models for piezoelectric transducers,” IEEE Trans. Ultrason., Ferroelect., Freq. Control, vol. 41, no. 1, pp. 60–66, Jan. 1994.
- [1.3.14] L. Capineri, L. Masotti, M. Rinieri, and S. Rocchi, “Ultrasonic transducer as a black-box: equivalent circuit synthesis and matching network design,” IEEE Trans. Ultrason., Ferroelect., Freq. Control, vol. 40, no. 6, pp. 694–703, Nov. 1993. Webster JG, *Medical instrumentation: application and design*, 2nd edn. Boston (Mass.), Houghton Mifflin, 1992.
- [1.3.15] J. A. Jensen, “Field: a program for simulating ultrasound systems,” Med. Biol. Eng. Comput., vol. 34, Suppl. 1, pt. 1, pp. 351–353, 1996.
- [1.3.16] F. Lindvall. The DREAM Toolbox. [Online]. Available: <http://www.signal.uu.se/Toolbox/dream/>
- [1.3.17] M. E. Frijlink, H. Kaupang, T. Varslot, and S.-E. Masøy. “Abersim: a simulation program for 3D nonlinear acoustic wave propagation for arbitrary pulses and arbitrary transducer geometries,” IEEE Ultrason. Symp., Nov. 2008, pp. 1282–1285.
- [1.3.18] S. Holm, “Ultrasim – A toolbox for ultrasound field simulation”, in Proc.

Nordic Matlab Conf. Oslo, Norway, Oct. 2001, pp. 1-5.

- [1.3.19] F. Varray, O. Basset, P. Tortoli, and C. Cachard, "CREANUIS: a nonlinear radio frequency ultrasound image simulator", *Ultrasound in Med. Biol.*, vol. 39, no. 10, pp. 1915-1924, 2013.
- [1.3.20] A. Ebadi, M. Mirzaie, and S. A. Gholamian, "A comparison between electrical circuit and finite element modeling methods for performance analysis of a three-phase induction motor under voltage unbalance," *Iran Journal of Electrical & Electronic Engineering*, vol. 8, no. 2, pp. 188-194 June 2012.
- [1.3.21] G. Matrone, A.S. Savoia, M. Terenzi, G. Caliano, F. Quaglia, and G. Magenes, "A volumetric CMUT-based ultrasound imaging system simulator with integrated reception and  $\mu$ -beamforming electronics models," *IEEE Trans. Ultrason., Ferroelect., Freq. Control*, vol. 61, no. 5, pp. 792-804, May. 2014.
- [2.1.1] W. R. Hedrick, D. L. Hykes, D. E. Starchman, "Ultrasound Physics and Instrumentation," Elsevier Mosby, 2005.
- [2.2.1] B. A. J. Angelsen, H. Torp, S. Holm, K. Kristoffersen, and T. A. Whittingham, "Which transducer array is best?" *Eur. J. Ultrasound*, vol. 2, no. 2, pp. 151-164, 1995.
- [2.3.1] J. Karki, "Signal Conditioning Piezoelectric Sensors", Texas Instrument Application Report, SLOA033A, Sept. 2000.
- [2.3.2] S.C. Cobbold, *Foundations of Biomedical Ultrasound*, Oxford University Press, 2007.
- [2.3.3] A. Arnau, *Piezoelectric Transducers and Application*, Berlin: Springer, 2008.
- [2.3.4] P.L.M.J. van Neer, *Ultrasonic Superharmonic Imaging*, PhD thesis: Department of Biomedical Engineering, Erasmus University, 2010.
- [2.3.5] P. Hoskins, K. Martin, A. Thrush, *Diagnostic Ultrasound Physics and Equipment*, Cambridge University Press, 2010.
- [3.1.1] W. P. Mason, *Electromechanical Transducers and Wave Filters*. New York: Van Nostrand, 1942.
- [3.1.2] D. Royer and E. Dieulesaint, *Ondes élastiques dans les solides*, Tome 2:



Génération, interaction acousto-optique, applications. Paris, France: Masson, 1999.

- [3.1.3] R. Krimholtz, D. A. Leedom, and G. L. Matthaei, "New equivalent circuits for elementary piezoelectric transducers," *Electron. Lett.*, vol. 6, no. 13, pp. 398–399, Jun. 1970.
- [3.1.4] A. Püttmer, P. Hauptmann, R. Lucklum, O. Krause, and B. Henning, "SPICE model for lossy piezoceramic transducer," *IEEE Trans. Ultrason., Ferroelectr., Freq. Control*, vol. 44, no. 1, pp. 60–66, Jan. 1997.
- [3.1.5] S. Morris and C. Hutchens, "Implementation of Mason's model on circuit analysis programs," *IEEE Trans. Ultrason., Ferroelectr., Freq. Control*, vol. UFFC-33, no. 3, pp. 295–298, May 1986.
- [3.1.6] J. Johansson and J. Delsing, "Effects of parasitic electrical components on an ultrasound system—Measurements and simulations using SPICE models," in *Proc. SPIE—Transducing Materials and Devices*, 2003, vol. 4946, pp. 174–182.
- [3.1.7] J. Johansson, "Optimization of a piezoelectric crystal driver stage using system simulations," in *Proc. IEEE Ultrason. Symp.*, 2000, vol. 2, pp. 1049–1054.
- [3.1.8] W. M. Leach, "Controlled-source analogous circuits and SPICE models for piezoelectric transducers," *IEEE Trans. Ultrason., Ferroelectr., Freq. Control*, vol. 41, no. 1, pp. 60–66, Jan. 1994.
- [3.1.9] P. C. Magnusson, G. C. Alexander and V. K. Tripathi, *Transmission Lanes and Wave Propagation*, 3rd edition. Boca Raton, FL: CRC Press. Inc., 1992.
- [3.1.10] A. R. Selfridge, "Approximate material properties in isotropic materials," *IEEE Trans. Ultrason., Ferroelectr., Freq. Contr.*, vol. 32, no. 3, pp. 381–394, May 1985.
- [3.1.11] J. van Deventer, T. Lofqvist, and J. Delsing, "PSpice simulation of ultrasonic systems," *IEEE Trans. Ultrason., Ferroelectr., Freq. Control*, vol. 47, no. 4, pp. 1014–1024, Jul. 2000.
- [3.1.12] R. Ludwig and P. Bretchko, *RF Circuit Design*. Upper Saddle River, NJ: Prentice-Hall, 2000.

- [3.1.13] J. Johansson, P.-E. Martinsson, and J. Delsing, "Simulation of absolute amplitudes of ultrasound signals using equivalent circuits," *IEEE Trans. Ultrason. Ferroelectr. Freq. Control*, vol. 54, no. 10, pp. 1977–1982, Oct. 2007.
- [3.2.1] H. Choi, H. Jung, H. C. Yang, F. Zheng, and K. K. Shung. "New Modified Butterworth Van-Dyke Model for High Frequency Ultrasonic Imaging," *IEEE Ultrason. Symp.*, Nov. 2012, pp. 576–579.
- [3.2.2] T. H. Lee, "The Design of CMOS Radio-Frequency Integrated Circuits," Cambridge, University Press, 2004.
- [3.3.1] L. Capineri, L. Masotti, M. Rinieri, and S. Rocchi, "Ultrasonic transducer as a black-box: equivalent circuit synthesis and matching network design," *IEEE Trans. Ultrason., Ferroelect., Freq. Control*, vol. 40, no. 6, pp. 694–703, Nov. 1993. Webster JG, *Medical instrumentation: application and design*, 2nd edn. Boston (Mass.), Houghton Mifflin, 1992.
- [3.3.2] S. Matsili-Libelli and M. Castelli, "An adaptive algorithm for numerical optimization," *Applied Mathematics and Computation*, vol. 23, pp. 341–357, 1987.
- [3.3.3] P. E. Gill, W. Murray, and M. H. Wright, *Practical Optimization*. London, U.K.: Academic Press, 1981, pp. 176–180.
- [3.3.4] G. R. Hams, "Hydrophone measurements in diagnostic ultrasound fields," *IEEE Trans. Ultrason., Ferroelect., Freq. Cont.*, vol. UFFC-35, pp. 87–101, 1988.
- [4.1.1] R. Reeder and C. Petersen, "The AD9271—A revolutionary solution for portable ultrasound," in *Analog Dialogue* 41–07. Norwood, MA, USA: Analog Devices Inc., Jul. 2007.
- [4.3.1] B. Gustavsen and A. Semlyen, "Rational approximation of frequency domain responses by vector fitting," *IEEE Trans. Power Del.*, vol. 14, no. 3, pp. 1052–1061, Jul. 1999..
- [4.3.2] R. Zeng and J. Sinsky, "Modified rational function modeling technique for high speed circuits," in *Proc. IEEE MTT-S Int. Microw. Symp. Dig.*, San Francisco, CA, USA, Jun. 11–16, 2006, pp. 1951–1954.

- [4.4.1] Quad  $\pm 90$  V,  $\pm 2$ A, 3/5 levels, High-speed Ultrasound Pulser, STMicroelectronics, Geneva, 2012, STHV748 DataSheet.
- [4.4.2] Fully integrated, 8-channel ultrasound analog front end with passive CW mixer, 0.75 nV/rtHz, 14/12-Bit, 65 MSPS, 153 mW/CH, Texas Instruments Inc., Dallas, TX, 2014, AFE5808 DataSheet.
- [4.4.3] S. Barra, A. Dendouga, S. Kouda, and N. Bouguechal, "Simulink behavioral modeling of a 10-bit pipelined ADC," J. Circuits Syst. Comput., vol. 22, no. 2, pp. 134–142, Feb. 2013.
- [5.1.1] L. Capineri, L. Masotti, M. Rinieri, and S. Rocchi, "Ultrasonic transducer as a black-box: equivalent circuit synthesis and matching network design," IEEE Trans. Ultrason., Ferroelect., Freq. Control, vol. 40, no. 6, pp. 694–703, Nov. 1993. Webster JG, Medical instrumentation: application and design, 2nd edn. Boston (Mass.), Houghton Mifflin, 1992.
- [5.1.2] L. Capineri, L. Masotti, M. Rinieri, and S. Rocchi, "Ultrasonic transducer as a black-box: equivalent circuit synthesis and matching network design," IEEE Trans. Ultrason., Ferroelect., Freq. Control, vol. 40, no. 6, pp. 694–703, Nov. 1993. Webster JG, Medical instrumentation: application and design, 2nd edn. Boston (Mass.), Houghton Mifflin, 1992.
- [5.1.3] Fully integrated, 8-channel ultrasound analog front end with passive CW mixer, 0.75 nV/rtHz, 14/12-Bit, 65 MSPS, 153 mW/CH, Texas Instruments Inc., Dallas, TX, 2014, AFE5808 DataSheet.
- [5.1.4] E. Brunner, "Ultrasound system considerations and their impact on front-end components," Analog Dialogue, Analog Devices Inc., vol. 36, no. 3, 2002.
- [5.2.1] S. S. Corbett III, "The influence of nonlinear fields on miniature hydrophone calibration using the planar scanning technique," IEEE Trans. Ultrason. Ferroelectr. Freq. Control, vol. 35, no. 2, pp. 162–167, Mar. 1988.
- [5.3.1] L. Svilainis, V. Dumbrava, "Evaluation of the ultrasonic transducer electrical matching performance," Ultrasound, vol. 62, pp. 16–21, 2007.

## 한글 초록

다양한 임상 응용 분야를 대응할 수 있는 초음파 시스템은 응용 분야에 따라 사용되는 트랜스듀서의 종류가 다르다. 각 트랜스듀서는 고유의 임펄스 응답 및 임피던스 특성을 가지고 있다. 임펄스 응답 특성은 송신하는 고전압 펄스의 모양과 에코 신호를 송신하는 프론트-엔드 일렉트로닉스의 성능을 결정한다. 그리고 임피던스 특성은 연결되는 트랜스듀서에 적합한 매칭 네트워크의 설계를 결정한다. 이러한 각 서브 시스템의 시스템 레벨에서의 최적화는 펄스-에코 (양방향) 응답 특성의 정확한 모델링이 요구되며, 이를 위해서는 초음파와 일렉트로닉스가 통합된 환경에서 시뮬레이션 되어야 한다.

본 논문은 의료 영상 진단을 위한 펄스-에코 초음파 시스템의 모델링 방법론을 제안하고, 이를 활용하여 매트랩/시뮬링크 환경에서 펄스-에코 초음파 시스템 시뮬레이터를 개발하였다.

이 시뮬레이터는 고전압 송신기, 송신 인터페이스, 초음파의 전달 및 반사를 포함하는 어쿠스틱 서브 시스템, 수신 인터페이스 그리고 프론트-엔드 송신기의 매트랩/시뮬링크 모델들로 통합하여 구현하였다.

제안하는 시뮬레이터의 유효성을 증명하기 위하여, 상용 초음파 시스템으로 얻어낸 측정된 데이터와 시뮬레이션 결과를 비교함으로써 모델의 실험적 검증

을 수행하였다. 제안하는 모델링 방법론 기반의 펄스-에코 초음파 시스템 시뮬레이터는 시스템 설계 변수의 최적화에 빠른 피드백을 얻어낼 수 있다.

**주요어:** 초음파 영상, 초음파 트랜스듀서, behavior modeling, 설계 최적화, 임피던스 매칭, MATLAB.

**학번:** 2012-30202